Computational Studies of 4H and 6H Silicon Carbide

by

Garrick Ng

A Dissertation Presented in Partial Fulfillment
of the Requirements for the Degree
Doctor of Philosophy

Approved November 2010 by the
Graduate Supervisory Committee:

Dieter Schroder, Chair
Dragica Vasileska
Brian Skromme
Terry Alford
Matthew Marinella

ARIZONA STATE UNIVERSITY

December 2010

ABSTRACT

Silicon carbide (SiC), long touted as a material that can satisfy the specific property requirements for high temperature and high power applications, was studied quantitatively using various techniques. The electronic band structure of 4H SiC is examined in the first half of this dissertation. A brief introduction to band structure calculations, with particular emphasis on the empirical pseudopotential method, is given as a foundation for the subsequent work. Next, the crystal pseudopotential for 4H SiC is derived in detail, and a novel approach using a genetic algorithm search routine is employed to find the fitting parameters needed to generate the band structure. Using this technique, the band structure is fitted to experimentally measured energy band gaps giving an indirect band gap energy of 3.28 eV, and direct Γ, M, K and L energy transitions of 6.30, 4.42, 7.90 and 6.03 eV, respectively. The generated result is also shown to give effective mass values of $m^*_{M\Gamma} = 0.66m_0$, $m^*_{M\mathrm{K}} = 0.31m_0$, $m^*_{M\mathrm{L}} = 0.34m_0$, in close agreement with experimental results.

The second half of this dissertation discusses computational work in finding the electron Hall mobility and Hall scattering factor for 6H SiC. This disscussion begins with an introductory chapter that gives background on how scattering rates are dervied and the specific expressions for important mechanisms. The next chapter discusses mobility calculations for 6H SiC in particular, beginnning with Rode's method to solve the Boltzmann transport equation. Using this method and the transition rates of the previous chapter, an acoustic deformation potential D_A value of 5.5 eV, an inter-valley phonon deformation potential D_{if} value of 1.25×10^{11} eV/m and inter-valley phonon energy $\hbar\omega_{if}$ of 65 meV that simultaneously fit experimental data on electron Hall mobility and Hall scattering factor was found.

ACKNOWLEDGMENTS

I would like thank my family and friends for their support and advice throughout my entire graduate school experience. In particular, I'd like to thank my sister for encouraging me to take the first steps down the path toward attaining a Ph.D.

In addition, I'd like to acknowledge all the assistance provided to me by everyone on my committee. I'd like to first thank Professor Schroder for his willingness to be my advisor, for providing me funding during my time at Arizona State University, and for allowing me to pursue my research interest. Above all, I'm grateful to him for putting up with me as I know that I may not be the easiest person to communicate with.

Just as importantly, I'm indebted to Professor Vasileska for all her encouragement and for her suggestions on possible research directions. Her suggestion of applying genetic algorithms to band structure calculations and her close review of my mobility calculations has been invaluable to my research success.

I'd also like to thank the remaining members on my committee – Dr. Marinella, Professor Skromme and Professor Alford – for taking their time to sit through my qualifying exam, comprehensive exam and dissertation defense. I'd like to also acknowledge the many enlightening discussions I've had with Dr. Marinella on his thoughts of open questions still remaining to be answered in experimental silicon carbide work, and the insight Professor Skromme gave me about the research done on the doping dependence of the ionization energy.

Finally, while not part of my committee, I'd like to thank Professor Ferry for going over a draft version of my dissertation, and for discussing with me his input on ways to improve it. In addition, I'd like to acknowledge his wonderful course in solid state physics, without which I would have never been introduced to the rich and deep subject of electronic band structure calculations.

TABLE OF CONTENTS

Page

Page

LIST OF TABLES

Table Page

LIST OF FIGURES

Figure Page

CHAPTER 1. INTRODUCTION

1.1. Introduction

Though a bedrock of the microelectronics industry for decades, bulk silicon (Si) as an electronic material is fast approaching many of its inherent limitations. The more highly publicized challenge facing Si is the extent to which devices on this material can be made smaller [1]. However, just as important is the challenge of developing devices which can operate under extreme conditions. For devices that are needed to function under high power, high temperature, or high radiation conditions, the family of silicon carbide (SiC) materials holds much promise [2-4].

The advantages of SiC over Si in the above mentioned areas have been much elucidated upon. The higher critical electric field of SiC compared with Si gives SiC a natural advantage in high power applications [3, 4]. Similarly SiC's large band gap energy, and consequently its lower intrinsic carrier concentration, as well as its higher thermal conductivity, makes it superior to Si as a high temperature material [2, 3]. On top of these superior qualities SiC, propitiously, can oxidize and form a silicon dioxide (SiO_2) insulating layer, allowing processing technology developed for Si to be applied to the development of SiC devices [2].

However, more still must be done in understanding the properties of SiC before it can be properly utilized in the electronics industry. Development of devices using SiC requires an understanding of the material's electronic transport properties, and that in turn begins with an understanding of the material's electronic band structure. With the electronic properties from the band structure known, various figures-of-merit important to transport, such as electron mobility, can be calculated. Therefore, this dissertation seeks to examine the electronic properties of SiC by first studying how the band structure is calculated and the parameters important to transport that can be deduced from it.

Subsequently, with the electronic parameters available from the band structure and knowledge of relevant scattering mechanisms, it will be shown how transport properties – specifically electron mobility in SiC – can be calculated.

1.2. Organization

In order accomplish the above stated goals, this dissertation will begin with a general overview of electronic band structures in chapter 2. This will proceed by first giving a brief history of the important developments in solid state physics over the last century. Next, the important results of the properties of electrons in a periodic potential are covered. Finally, a general description of the empirical pseudopotential method (EPM), with which the band structure of SiC will be calculated in the following chapter, is given.

In chapter 3, the band structure of SiC will be calculated and discussed. The topic will be introduced by first describing the various polytypes of SiC and their crystal structures. Next, the details of the EPM applied specifically to 4H-SiC and a fitting routine based on a genetic algorithm to calculate the band structure is discussed. Finally, the results of the calculation are presented, along with the relevant parameters that can be extracted from the band structure.

With the band structure examined in the previous two chapters, the second half of this dissertation will move on to examine how the electron mobility and Hall mobility can be calculated. This will begin in chapter 4, where the general principles of scattering are introduced. The central result of scattering theory, Fermi's Golden Rule, will be derived. Following this, the expressions that various scattering mechanisms take on are given.

Chapter 5 will cover the mobility properties of SiC specifically. First, a survey of previous experimental and computational work of SiC will be given. Next will be a discussion of how the scattering mechanisms discussed in the previous chapter can be used to calculate electron mobility and Hall mobility. This is followed by an analysis of

the important scattering mechanisms in 6H SiC SiC. Electron mobility and Hall mobility calculations for 6H-SiC will be presented. Finally, a brief investigation of how the decrease of the ionization energy with doping concentration affects the mobility will be covered.

Chapter 6 will conclude this dissertation and provide a summary of the work. Suggestions for improvements and future directions will also be given.

CHAPTER 2. ELECTRONIC BAND STRUCTURE THEORY

2.1. Introduction

At the turn of the last century, Drude proposed his highly successful theory of electrical conduction [5]. This model, still in use in the semiconductor industry to this day, applied the kinetic theory of dilute gases to electrons in a metal. Using this approach, many of the observed phenomena in metals, such as Ohm's Law and the Hall effect, could be explained. A further refinement came with Sommerfeld's modification of Drude's theory. By using the Fermi-Dirac distribution in calculating thermodynamic quantities of the electron gas, Sommerfeld resolved many of the anomalous thermal results in Drude's model. Despite all its successes, the free electron gas model still exhibited many troubling deficiencies. Among the most glaring inadequacies of the free electron gas model was its inability to explain the cubic temperature dependence of the intermediate-temperature specific heat of metals. Nor could the free electron model explain why some electrons conducted, while others remained bound to their ions.

The source of the deficiencies in the models of Drude and Sommerfeld originated from the assumption that electrons moved free of any potential in a material. This was a very crude assumption, and disproven by the 1913 experimental work of W. and L. Bragg which demonstrated that solids possessed an underlying crystalline structure at the microscopic level [5]. The regular arrangement of atoms subject electrons to a periodic potential, a situation that leads to the quantization of the energy levels of the electrons. Using this new picture of electrons confined by the potential of the crystal lattice, many phenomena unexplainable by the free electron gas model could be resolved.

2.2. Hamiltonian of a Crystalline Solid

In order to solve the problem of electrons confined in the periodic potential of a solid, quantum mechanics must be invoked. The relevant Hamiltonian to be solved in this case

is given by

$$H = \sum_i \frac{p_i^2}{2m_0} - \sum_j \frac{P_j^2}{2M_j} - \sum_{i,r\neq i} \frac{q_i q_r}{4\pi\varepsilon_0 x_{ir}} - \sum_{j,s\neq j} \frac{Q_j Q_s}{4\pi\varepsilon_0 x_{js}} + \sum_{i,j} \frac{q_i Q_j}{4\pi\varepsilon_0 x_{ij}} \quad (2.1)$$

where q_i and q_j are the charge of the of the *i*th and *j*th electron, respectively, Q_j and Q_s are the charge of the *j*th and *s*th nucleus, respectively, x_{ir} is the distance between electrons, x_{js} is the distance between nuclei, x_{ij} is the distance between the *i*th electron and *j*th nucleus, $\boldsymbol{p}_i$ is the momentum operator for the *i*th electron, $\boldsymbol{P}_j$ is the momentum operator of the *j*th nucleus, ε_0 is the permittivity of free space, m_0 is the rest mass of an electron, and M_j is the mass of the *j*th nucleus [6]. In this equation, the first and second terms represent the kinetic energies of the electrons and ions, respectively, the third term the potential energy between electrons, the fourth term the potential energy between ions, and the last term the potential energy between electrons and ions. This many-electron problem would be impossible to solve directly for any solid of macroscopic size, and therefore many simplifying assumptions must be made.

The first of the approximations to be made is based on the observation that electrons are many orders of magnitude less massive than the ions in a solid. Therefore, electrons move much faster than ions, vibrating at a frequency on the order of 10^{15} s^{-1} compared to 10^{13} s^{-1} for ions [6]. Electronic motion therefore responds almost instantaneously to ionic motion, while ions only experience a time-averaged electronic potential. This is known as the Born-Oppenheimer or adiabatic approximation, and allows the Hamiltonian to be written in three separate terms as

$$H = H_{ion} + H_{el} + H_{el-ion} \quad (2.2)$$

where H_{ion} is the Hamiltonian for the ionic motion due to the ionic potential and the time-averaged electronic potential, H_{el} is the Hamiltonian for the electrons with the nuclei frozen in their equilibrium position, and H_{el-ion} is the Hamiltonian of the change in electronic energies with changes in the positions of the ions.

The electronic Hamiltonian is the system of interest, and this is given by

$$H_{el} = \sum_i \frac{p_i^2}{2m_0} - \sum_{i,r\neq i} \frac{q_i q_r}{4\pi\varepsilon_0 x_{ir}} + \sum_{i,j} \frac{q_i Q_j}{4\pi\varepsilon_0 x_{ij}} \qquad (2.3).$$

This portion of the Hamiltonian would still be impractical to solve given that there are more than 10^{23} electrons/cm^3 in a solid. A further assumption known as the mean-field approximation is made by assuming every electron is subjected to the same average potential. Separating the electron-electron interaction term into one that only involves electrons closely bound to ions and one that only involves bonding electrons, the Hamiltonian becomes

$$\begin{aligned}
H_{el} &= \sum_i \frac{p_i^2}{2m_0} - \sum_{i,r\neq i} \frac{q_i q_r}{4\pi\varepsilon_0 x_{ir}} + \sum_{i,j} \frac{q_i Q_j}{4\pi\varepsilon_0 x_{ij}} \\
&= \sum_i \left[\frac{p_i^2}{2m_0} + \sum_j \frac{q_i Q_j}{4\pi\varepsilon_0 x_{ij}} \right] - \sum_{i,r\neq i} \frac{q_i q_r}{4\pi\varepsilon_0 x_{ir}} \\
&= \sum_i \left[\frac{p_i^2}{2m_0} + \sum_j \frac{q_i Q_j}{4\pi\varepsilon_0 x_{ij}} \right] - \sum_{i,r\subset bound} \frac{q_i q_r}{4\pi\varepsilon_0 x_{ir}} - \sum_{i,r'\neq i} \frac{q_i q_r}{4\pi\varepsilon_0 x_{ir'}} \\
&= \sum_i \left[\frac{p_i^2}{2m_0} + q_i \left\{ \sum_j \frac{Q_j}{4\pi\varepsilon_0 x_{ij}} - \sum_{r\subset bound} \frac{q_r}{4\pi\varepsilon_0 x_{ir}} \right\} \right] \\
&\quad - \sum_{i,r'\neq i} \frac{q_i q_r}{4\pi\varepsilon_0 x_{ir'}} \\
&\approx \sum_i \left[\frac{p_i^2}{2m_0} + V(\boldsymbol{r}) \right] - \sum_{i,r'\neq i} \frac{q_i q_r}{4\pi\varepsilon_0 x_{ir'}} \qquad (2.4)
\end{aligned}$$

where $V(\boldsymbol{r})$ is the average potential felt by each electron. The replacement of the exact electron-ion and bound electron-electron interaction by $V(\boldsymbol{r})$ is known as the mean-field approximation. Furthermore, by ignoring the bonding electron-electron interaction term, the Hamiltonian reduces to a one-electron problem given by

$$H_{1el}\Phi_{\mathrm{n}}(\boldsymbol{r}) = \left(\frac{p^2}{2m_0} + V(\boldsymbol{r})\right)\Phi_n(\boldsymbol{r}) = E_n\Phi_n(\boldsymbol{r}) \tag{2.5}$$

where H_{1el} is the one-electron Hamiltonian, and $\varphi(\boldsymbol{r})$ and E_n are the one-electron wave function and energy of eigenstate n, respectively.

2.3. Bloch Functions

The consequence of subjecting an electron to the periodic potential of the crystal lattice was first elucidated by Bloch. Solutions to the one-electron Schrödinger equation in Eq. (2.4) take on a special form, known as Bloch functions. Using these Bloch functions, any general solution to (2.4) can be formed by taking a linear combination of the aforementioned functions.

To arrive at the Bloch function solutions, a translational operator T_R is first defined for a Bravais lattice vector $\boldsymbol{R}$ and any function $f(\boldsymbol{r})$ such that

$$T_R f(\boldsymbol{r}) = f(\boldsymbol{r} + \boldsymbol{R}) \tag{2.6}$$

Solutions to the operator T_R can be expressed in the form of

$$\varphi_{\boldsymbol{k}}(\boldsymbol{r}) = e^{i\boldsymbol{k}\cdot\boldsymbol{r}}u_{\boldsymbol{k}}(\boldsymbol{r}) \tag{2.7}$$

where $u_{\boldsymbol{k}}(\boldsymbol{r})$ are functions with the same periodicity as that of the lattice. For any integer *n* then,

$$u_{\boldsymbol{k}}(\boldsymbol{r}) = u_{\boldsymbol{k}}(\boldsymbol{r} + n\boldsymbol{R}) \tag{2.8}$$

which are cell periodic functions of the crystal. The result of T_R operating on $\varphi_{\boldsymbol{k}}(\boldsymbol{r})$ is

$$T_R\varphi_{\boldsymbol{k}}(\boldsymbol{r}) = \varphi(\boldsymbol{r}+\boldsymbol{R}) = e^{i\boldsymbol{k}\cdot\boldsymbol{R}}\varphi_{\boldsymbol{k}}(\boldsymbol{r}) = \varphi_{\boldsymbol{k}}(\boldsymbol{r}) \tag{2.9}$$

since $\boldsymbol{k}\cdot\boldsymbol{R}$ is some multiple of 2π. The one-electron Hamiltonian H_{1el} is also invariant under translation by $\boldsymbol{R}$, and therefore the operators H_{1el} and T_R commute. As a consequence, quantum mechanics dictate that the eigenfunctions of T_R are also eigenfunctions of H_{1el}. Any solution to the one-electron Schrödinger equation Eq. (2.4) can therefore be expressed as a linear combination of Bloch functions

$$\Phi(\boldsymbol{r}) = \sum_{\boldsymbol{k}} A_{\boldsymbol{k}}\varphi_{\boldsymbol{k}}(\boldsymbol{r}) = \sum_{\boldsymbol{k}} A_{\boldsymbol{k}}e^{i\boldsymbol{k}\cdot\boldsymbol{r}}u_{\boldsymbol{k}}(\boldsymbol{r}) \tag{2.10}$$

where $A_{\boldsymbol{k}}$ are the expansion coefficients.

2.4. Empirical Pseudopotential Method

While the form of the electronic wave functions are in principle Bloch functions, further simplifications are needed to efficiently calculate the electronic band structure. One of the more commonly used techniques used in practical calculations is known as the empirical pseudopotential method. In this approach, electrons are divided into two groups – the core and the valence electrons. The core electrons are those that occupy orbitals of completely filled shells, while the valence electrons are those that occupy orbitals of partially filled shells. The core electrons are tightly bound to their respective nuclei and therefore localized around their lattice sites. These electrons do not contribute to bonding or conduction, and are not dealt with. Only the valence electrons, which are weakly bound and nearly free, that are involved in bonding and transport are considered.

In order to further ease the solving of the wave equation, the valence electron wave functions can be divided into two parts. The parts of the wave equation away from the core are smooth, and can be approximated with a reasonable number of plane waves.

Those parts close to the core exhibit rapid spatial oscillations, making the wave function difficult to approximate. However at the same time, these rapid oscillations in the wave function serve to screen the strong Coulomb potential of the atomic sites, leaving behind a much weaker "pseudopotential." Ultimately, the hope is that the pseudopotential is sufficiently small that it justifies treating the electrons as nearly free, and therefore appropriate to approximate the valence electron wave functions with a small number of plane waves.

This replacement of the true potential with the pseudopotential in the one-electron Schrödinger equation leads to the pseudo-wave equation

$$\left(\frac{p^2}{2m_0} + V_{PS}(\boldsymbol{r})\right)\Psi_{\boldsymbol{k}} = E_{\boldsymbol{k}}\Psi_{\boldsymbol{k}} \tag{2.11}$$

where $\Psi_{\boldsymbol{k}}$ is the pseudo-wave function to be expanded in a basis of plane waves. The expansion of $\Psi_{\boldsymbol{k}}$ is given by

$$\Psi_{\boldsymbol{k}}(\boldsymbol{r}) = \frac{e^{i\boldsymbol{k}\cdot\boldsymbol{r}}}{\sqrt{\Omega}}\sum_{\boldsymbol{G}} C_{\boldsymbol{k}} e^{i\boldsymbol{G}\cdot\boldsymbol{r}} \tag{2.12}$$

where the vectors $\boldsymbol{G}$ are the reciprocal lattice vectors, the $C_{\boldsymbol{k}}$'s are the expansion coefficients and Ω is the volume of the unit cell. The reciprocal lattice vector $\boldsymbol{G}$ is defined as

$$\boldsymbol{G} = n_1\boldsymbol{b}_1 + n_2\boldsymbol{b}_2 + n_3\boldsymbol{b}_3 \tag{2.13}$$

where $\boldsymbol{b}_i$ are the reciprocal primitive vectors for the crystal and n_i are integers. The inner product of Eq. (2.11) using the wave function of Eq. (2.12) leads to the secular equation

$$det\left|\left[\frac{\hbar^2}{2m_0}|\boldsymbol{k}+\boldsymbol{G}|^2 - E_{\boldsymbol{k}}\right]\delta_{\boldsymbol{G},\boldsymbol{G}'} + V_{\boldsymbol{G},\boldsymbol{G}'}\right| = 0 \tag{2.14}$$

whose solutions are the energy eigenvalues $E_{\boldsymbol{k}}$. The off-diagonal matrix elements of the pseudopotential $V_{\boldsymbol{G},\boldsymbol{G}'}$ are given by

$$V_{G,G'} = \frac{1}{\Omega}\int V_{PS}(\boldsymbol{r})e^{i(\boldsymbol{G}'-\boldsymbol{G})\cdot\boldsymbol{r}}\,d\boldsymbol{r} \tag{2.15}$$

which is just the Fourier transform of the pseudopotential, and are known as pseudopotential form factors. However, this expression only accounts for one atom per unit cell. If more than one atom exists within the unit cell, an additional term must be included to account for the different kinds and the different positions of the other atoms. The pseudo potential then becomes

$$V_{PS}(\boldsymbol{r}) = \sum_{\boldsymbol{G}'-\boldsymbol{G}} V_{G'-G,\alpha}\, S_{\boldsymbol{G}'-\boldsymbol{G},\alpha} e^{i(\boldsymbol{G}'-\boldsymbol{G})\cdot\boldsymbol{r}} \tag{2.16}$$

where $V_{\boldsymbol{G}'-\boldsymbol{G},\alpha}$ is the pseudopotential form factor for atoms of species α and $S_{\boldsymbol{G}'-\boldsymbol{G},\alpha}$ is the structure factor which accounts for the positions of those atoms. The structure factor is given by

$$S_{\boldsymbol{G}'-\boldsymbol{G},\alpha} = \frac{1}{N_\alpha}\sum_j e^{-i(\boldsymbol{G}'-\boldsymbol{G})\cdot\boldsymbol{r}_{\alpha j}} \tag{2.17}$$

where N_α is the number of atoms of species α and $\boldsymbol{r}_{\alpha j}$ is a vector pointing to the location of the *j*th α atom.

As stated before, there exist many different methods to determine the pseudopotential matrix elements of Eq. (2.15). One approach is to directly calculate it using an approximation for the atomic potential $V_{PS}(\boldsymbol{r})$. An example of this is the empty-core potential due to Ashcroft which is a spherically symmetric potential that is zero up to a critical radius, then a screened Coulomb potential thereafter [7]. This is given by the expression [8]

$$V_{PS}(\boldsymbol{r}) = V_0 e^{-r/d} \frac{\Omega}{4\pi d^3} \frac{d}{r} \Theta(r - R_c) \tag{2.18}$$

where V_0 is the magnitude of the potential, d is the screening length, R_c is the critical radius, and $\Theta(x)$ is the step function. The Fourier transform found using Eq. (2.15) is then [8]

$$V_{G,G'} = V_0 e^{-R_c/d} \frac{\sin(R_c|\boldsymbol{G'} - \boldsymbol{G}|) + |\boldsymbol{G'} - \boldsymbol{G}| d \cos(R_c|\boldsymbol{G'} - \boldsymbol{G}|)}{d|\boldsymbol{G'} - \boldsymbol{G}|[d^2|\boldsymbol{G'} - \boldsymbol{G}|^2 + 1]} \tag{2.19}.$$

As an example, the pseudopotential and its Fourier transform for the case of aluminum (Al) is shown in Fig. 2.1. In addition, first-principles pseudopotentials can be constructed for the atom under consideration. This is done by solving the Schrödinger equation for the radial wave functions of the outermost electrons, then finding the pseudopotential that gives a pseudo wave function that matches the smooth portion of the said radial wave function. Finally, a fully empirical approach would be to use the pseudopotential matrix elements as fitting variables. This is the approach taken in this dissertation, and will be outlined in the next chapter.

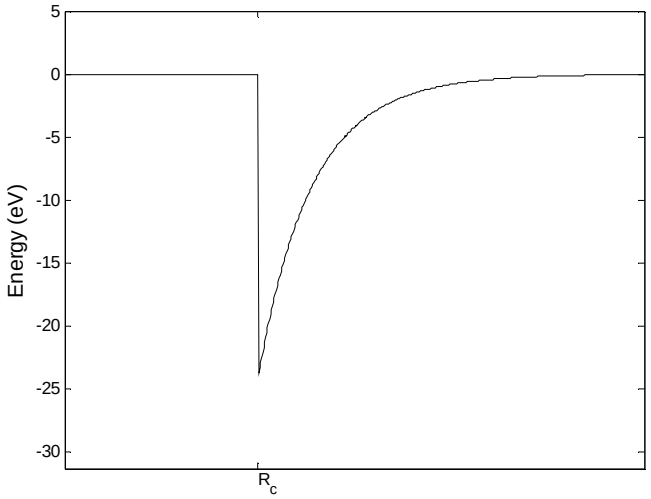

(a)

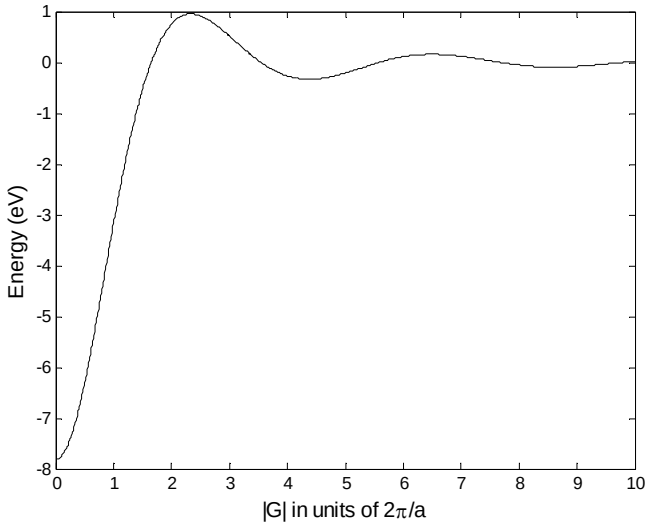

(b)

Fig. 2.1. The Al pseudopotential (a) and its Fourier transform (b), with $a = 4.05 \times 10^{-8}\ cm$, $U_0 = 31.3\ eV$, $d = 0.35 \times 10^{-8}\ cm$, and $R_c = 0.943 \times 10^{-8}\ cm$.

CHAPTER 3. ELECTRONIC BAND STRUCTURE OF 4H SIC

3.1. Introduction

Studies of the band structure of SiC began not long after the development of a process to grow single crystals of the material. The first comprehensive study of the band structure of the various polytypes of SiC was done in 1970 by Junginger and van Haeringen [9]. This was done with the EPM technique discussed last chapter, using the pseudopotentials of silicon (Si) and carbon (C) with the hopes that they were transferable with minor modifications. Because of the lack of computing power at that time, the full bands were only calculated for 3C and 2H polytypes of SiC. For the 4H and 6H, only the energies at the high-symmetry points were calculated. While the calculated energy band gaps for the 3C and 2H matched well with experiment, the results were not so successful for the hexagonal phases with larger basis sets.

As is common when investigating new materials, several other calculations approached the problem from a more complete first principles perspective. Gavrilenko *et al*. made calculations for the 4H and 6H polytypes using a self-consistent linear muffin-tin orbital method with greater success in matching the energy gaps in 6H than 4H [10]. A local density approximation (LDA) of the density functional theory (DFT) was adopted in a band structure calculation by Persson and Lindefelt to match the experimental effective masses in 3C, 2H, 4H and 6H SiC [11]. While successful in the goal of calculating the effective masses, the resulting energy band gaps were off from the experimental values by a great deal. More successful first principles calculations in terms of more accurate energy band gaps were performed by Wenzien *et al*. using a quasiparticle approach [12] and Baumeier *et al*. using a DFT approach but with electron self-interactions taken into account [13].

While these last two *ab initio* calculations are fairly accurate given the current knowledge of the energy band gaps and the effective masses, they are computationally expensive to implement. In addition, any new experimental data on the band structure that do not fit values given by current calculations require further research to find the source of the discrepancies. For this reason, empirical or semi-empirical approaches such as the EPM or the tight-binding method are preferable when experimental data are available. As stated above, the study of Junginger and van Haeringen relied on a semi-empirical approach to the EPM. More recently, Pennington and Goldsman also used the EPM to calculate the band structure of 3C, 4H, and 6H SiC [14]. This study obtained better results in terms of fitting the energy band gap and the electron effective masses by introducing nonlocal screening effects into the pseudopotentials of Si and C. The approach was also semi-empirical in that it relied on the transferability of the Si and C atomic potentials, with modifications to account for the aforementioned screening effects. Zubkova *et al.* also used the semi-empirical EPM, based on the same pseudopotentials used by Junginger *et al.*, to study the temperature dependence of the band structure [15]. In contrast, the empirical approach to the EPM is to abandon attempts to obtain the form factors from the atomic potentials and instead treat the Fourier coefficients as completely adjustable parameters to match experimental band structure data.

The flexibility offered by the empirical or semi-empirical approaches is especially important for 4H SiC since the experimental work on its band structure is still sparse. To date, only a few experimental studies have been performed to investigate the electronic structure of 4H SiC. The indirect, Γ to M band gap energy of 4H SiC was first measured by Choyke *et al.*, for which a value of 3.263 eV was obtained [16]. This is still the most widely quoted experimental value for the band gap energy to this day [12-14]. Optical measurements by Ahuja *et al.* gave the direct gap energies at the Γ, M, K and L high

symmetry points as 6.2, 4, 7.8 and 6.7 eV, respectively, and a total valence band energy of 18.2 eV [17]. Electroreflectance measurements by Demir *et al.* supported those values, giving the direct gap energy at the Γ and M points as 6.18 and 4.5 eV, respectively [18]. Compared with this experimental data, the band structure of Pennington *et al.* underestimates the direct Γ transition by more than 1 eV and overestimates the direct M transition by about the same amount. The calculation by Zubkova *et al.* also has many deviations from experiment, with a band gap energy smaller by about 0.3 eV, a direct Γ transition smaller by 1.6 eV and a direct L transition smaller by more than 1.5 eV.

In this chapter, an empirical approach is demonstrated to better fit the direct band gap energies. The fitting will be done specifically for the 4H polytype for which there is a relative abundance of experimental data to fit to. The next section will begin by briefly giving an overview of the different polytypes of SiC, and then describe in detail the crystal structure of the 4H polytype. The derivation of the form factors for 4H SiC will then follow, and a description of the fitting routine used will be given. Finally, the results of the fitted band structure will be presented.

3.2. Crystal Structures of Silicon Carbide

Silicon carbide is among a special class of materials that exhibit a property known as polytypism. This means that, while all polytypes of SiC are chemically identical, they can crystallize into more than one stable crystal structure. There are more than a hundred known polytypes of SiC broadly categorized as either being α-SiC or β-SiC. These categorizations indicate whether the structure is cubic (β-SiC) or non-cubic (α-SiC). Only the 3C polytype, which crystallizes into a cubic, zinc-blende structure similar to gallium arsenide (GaAs), falls into the category of β-SiC. All other polytypes are ambiguously labeled as α-SiC. The crystal structures of SiC can be described as being

made up of layers of atoms that are in a close-packed hexagonal structure [19]. This structure can be described as a plane of atoms arranged in a honeycomb lattice, and can be visualized by packing identical hard spheres as shown in Fig. 3.1. Various crystal structures can be constructed by stacking these layers of atoms upon one another. Because of energy considerations, there are no examples of an element with a crystal structure where one close-packed hexagonal layer is stacked directly above another. Instead, subsequent layers are stacked so that they occupy the interstices in the preceding layers. Layers stacked in this way have two distinct possible sets of interstices with respect to the first layer. These possibilities are shown in Fig. 3.1 with the sets of positions labeled B and C.

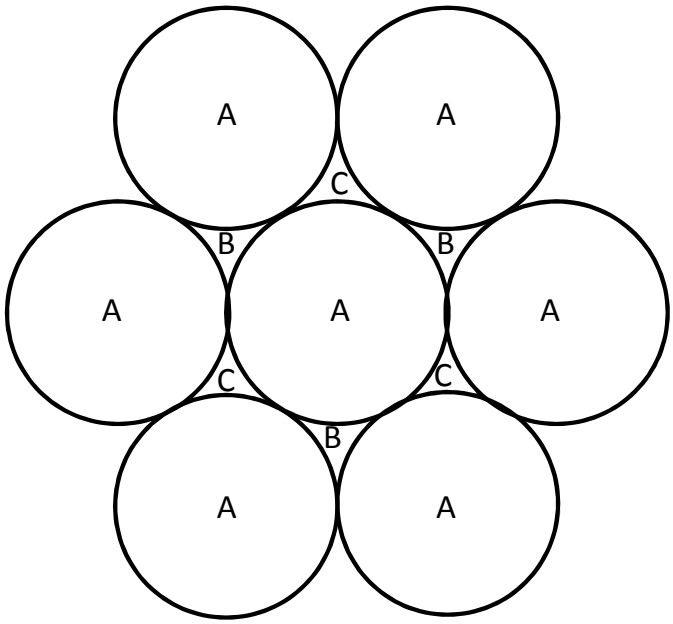

Fig. 3.1. Close-packed hexagonal layer showing the three unique possible sets of lattice sites.

With these three different positions for each layer, an infinite number of different

structures can be formed depending on the number of layers and the order in which they are stacked. For example, a structure can be created by stacking layers of atoms in a two-layer repeat, ABAB fashion creating a hexagonal close packed (hcp) lattice. Stacking layers in a three-layer repeat, ABCABC fashion creates a face centered cubic (fcc) lattice. The stacking sequence of the layers therefore defines the crystal structure.

In the various polytypes of SiC, instead of layers made of single atoms, at each lattice site there is set of two atoms – one Si, one C. These layers are stacked in the same manner as described in the preceding paragraph. The stacking order and resultant crystal structure formed in the SiC polytypes is identified using a special notation known as Ramsdell Notation. In this system, each polytype is labeled by a number indicating the period of the stacking sequence, and a letter indicating the Bravais lattice to which the polytype belongs. For instance, hcp structure ABAB would be denoted by 2H to indicate the two-layer repeat and hexagonal structure. The β-SiC structure with stacking sequence ABCABC would be denoted by 3C to indicate the three-layer repeat and cubic structure. For the 4H polytype, which this chapter focuses upon, the stacking sequence is a four-layer repeat given by ABCBABCB. This is shown in Fig. 3.2a, which illustrates the sequence of layers with the two atom basis.

3.3. Crystal Pseudopotential for 4H SiC

As discussed in the previous chapter, the off-diagonal elements of the Hamiltonian are crystal structure dependent. From Eq. 2.14, the pseudopotential matrix elements are

$$V_{\mathbf{G},\mathbf{G}'} = \frac{1}{\Omega}\int \sum_{j=1}^{4}\left[V_a(\boldsymbol{r}-\boldsymbol{r}_{aj}) + V_b(\boldsymbol{r}-\boldsymbol{r}_{bj})\right]e^{i(\boldsymbol{G}'-\boldsymbol{G})\cdot\boldsymbol{r}}\,d\boldsymbol{r}$$

$$= \frac{1}{\Omega}\int \sum_{j=1}^{4}\left[V_a(\boldsymbol{r})e^{-i(\boldsymbol{G}'-\boldsymbol{G})\cdot\boldsymbol{r}_{aj}} + V_b(\boldsymbol{r})e^{-i(\boldsymbol{G}'-\boldsymbol{G})\cdot\boldsymbol{r}_{bj}}\right]e^{i(\boldsymbol{G}'-\boldsymbol{G})\cdot\boldsymbol{r}}\,d\boldsymbol{r} \quad (3.1)$$

where subscript a indicates *a* Si atom, subscript *b* indicates a C atom, $\boldsymbol{r}_{aj}$ is the position of the *j*th Si atom, and $\boldsymbol{r}_{bj}$ is the position of the *j*th C atom. To find the form of this structure dependent term, the crystal structure of the 4H SiC lattice is analyzed in Fig. 3.2b where the locations in first quadrant of the *xy*-plane of the atoms in each layer is indicated.

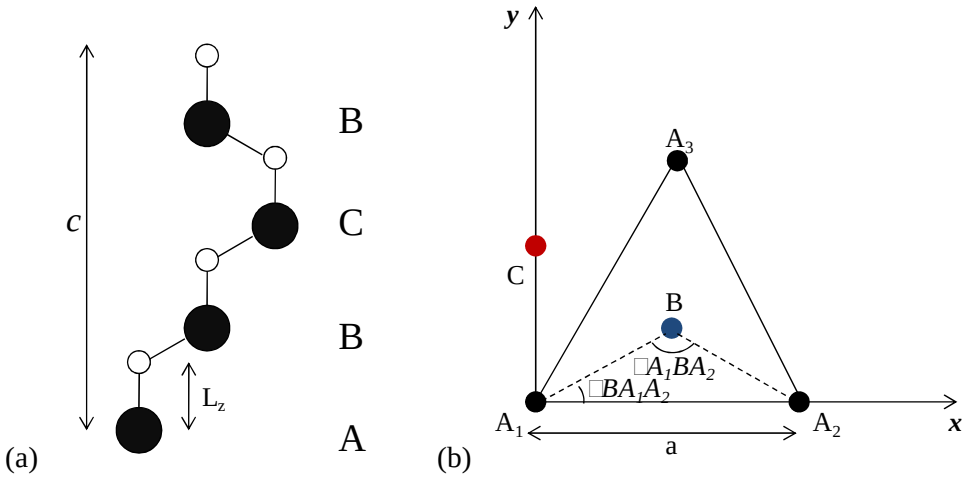

Fig. 3.2. (a) Stacking sequence of the 4H SiC polytype showing the eight atom basis set. The black circles represent Si atoms, while the white circles represent C atoms. (b) Locations of the A, B and C layer lattice sites in the first quadrant of the *xy*-plane.

The underlying Bravais lattice of 4H SiC is hexagonal, which can be described by stacking close-packed hexagonal layers directly above one another. The real space translation vectors that describe the hexagonal system can be obtained by taking a lattice point in the A layer arbitrarily as the origin (A_1 in Fig. 3.2b). Since the symmetry of each layer is close-packed hexagonal, the angle $\angle A_2A_1A_3$ is $\pi/3$ and each nearest neighbor lattice site is separated by a lattice constant *a*. Therefore, lattice sites A_2 and A_3 are located at $a\hat{\boldsymbol{x}}$ and $(a/2)\hat{\boldsymbol{x}} + (\sqrt{3}a/2)\hat{\boldsymbol{y}}$, respectively. The layer stacked directly above

can be described by translating a lattice constant *c* in the *z* direction. This gives the three translation vectors as

$$\boldsymbol{a}_1 = a\hat{\boldsymbol{x}} \tag{3.2},$$

$$\boldsymbol{a}_2 = (a/2)\hat{\boldsymbol{x}} + \left(\sqrt{3}a/2\right)\hat{\boldsymbol{y}} \tag{3.3},$$

and

$$\boldsymbol{a}_3 = c\hat{\boldsymbol{z}} \tag{3.4}.$$

The reciprocal lattice vectors corresponding to this set of real space translation vectors are

$$\boldsymbol{b}_1 = 2\pi\frac{\boldsymbol{a}_2 \times \boldsymbol{a}_3}{\boldsymbol{a}_1 \cdot \boldsymbol{a}_2 \times \boldsymbol{a}_3} = \frac{2\pi}{a}\hat{\boldsymbol{x}} - \frac{2\pi}{a\sqrt{3}}\hat{\boldsymbol{y}} \tag{3.5},$$

$$\boldsymbol{b}_2 = 2\pi\frac{\boldsymbol{a}_3 \times \boldsymbol{a}_1}{\boldsymbol{a}_1 \cdot \boldsymbol{a}_2 \times \boldsymbol{a}_3} = -\frac{4\pi}{a\sqrt{3}}\hat{\boldsymbol{y}} \tag{3.6},$$

and

$$\boldsymbol{b}_3 = 2\pi\frac{\boldsymbol{a}_1 \times \boldsymbol{a}_2}{\boldsymbol{a}_1 \cdot \boldsymbol{a}_2 \times \boldsymbol{a}_3} = -\frac{2\pi}{c}\hat{\boldsymbol{z}} \tag{3.7}.$$

For the specific case of the 4H structure with an ABCB stacking sequence, the B and C lattice sites in the *xy*-plane are located in the interstices between the A atoms, equidistant from each. The first B layer is translated from the A layer in the *z* direction by *c*/4, while the second B layer is translated by 3*c*/4. Because the B atom is equidistant from each A atom in the *xy*-plane, and since the distance between each A atom is *a*, the angle $\angle A_1BA_2$ is $2\pi/3$. The angles $\angle BA_1A_2$ and $\angle BA_2A_1$ must then be $\pi/6$, making ΔA_1BA_2 isosceles. Therefore, the B lattice sites are located at $(a/2)\hat{\boldsymbol{x}} + \left(a/2\sqrt{3}\right)\hat{\boldsymbol{y}}$ in

the *xy*-plane. Finally, the C lattice site in the xy-plane is located in the interstices between lattice sites A_1, A_2, and a site in the second quadrant which is the reflection of A_2 across the *y*-axis. Since the distance between A_1 and B is $(a/\sqrt{3})$, the location of the C lattice site is $(a/\sqrt{3})\hat{\boldsymbol{y}} + (c/2)\hat{\boldsymbol{z}}$ relative to the origin.

As stated previously, each lattice point in SiC is composed of a Si and a C atom separated by a bond length of L_z (see Fig. 3.2a). In order to make calculations easier, the origin can be arbitrarily shifted to the midpoint of the two atoms so that $\boldsymbol{r}_{a1} = -\boldsymbol{s} = (-L_z/2)\hat{\boldsymbol{z}}$ and $\boldsymbol{r}_{b1} = \boldsymbol{s} = (L_z/2)\hat{\boldsymbol{z}}$. Substituting this into Eq. (3.1)

$$V_{\boldsymbol{G},\boldsymbol{G}'} = \frac{1}{\Omega}\int \left(V_a(\boldsymbol{r})e^{i(\boldsymbol{G}'-\boldsymbol{G})\cdot\boldsymbol{s}} + V_b(\boldsymbol{r})e^{-i(\boldsymbol{G}'-\boldsymbol{G})\cdot\boldsymbol{s}}\right)e^{i(\boldsymbol{G}'-\boldsymbol{G})\cdot\boldsymbol{r}}\sum_{j=1}^{4} e^{-i(\boldsymbol{G}'-\boldsymbol{G})\cdot\boldsymbol{r}_j}\, d\boldsymbol{r}$$

$$= \frac{1}{\Omega}\int \left[V_a(\boldsymbol{r})\left(\cos\left((\boldsymbol{G}'-\boldsymbol{G})\cdot\boldsymbol{s}\right) + i\sin\left((\boldsymbol{G}'-\boldsymbol{G})\cdot\boldsymbol{s}\right)\right)\right.$$

$$\left. + V_b(\boldsymbol{r})\left(\cos\left((\boldsymbol{G}'-\boldsymbol{G})\cdot\boldsymbol{s}\right) - i\sin\left((\boldsymbol{G}'-\boldsymbol{G})\cdot\boldsymbol{s}\right)\right)\right]e^{i(\boldsymbol{G}'-\boldsymbol{G})\cdot\boldsymbol{r}}d\boldsymbol{r} \times \sum_{j=1}^{4} e^{-i(\boldsymbol{G}'-\boldsymbol{G})\cdot\boldsymbol{r}_j}$$

$$= \left[V_{\boldsymbol{G}}^{S}\cos\left((\boldsymbol{G}'-\boldsymbol{G})\cdot\boldsymbol{s}\right) + iV_{\boldsymbol{G}}^{A}\sin\left((\boldsymbol{G}'-\boldsymbol{G})\cdot\boldsymbol{s}\right)\right]\sum_{j=1}^{4} e^{-i(\boldsymbol{G}'-\boldsymbol{G})\cdot\boldsymbol{r}_j} \qquad (3.8)$$

where $\boldsymbol{r}_j$ is the position of the midpoint of the basis set in each layer, and $V_{\boldsymbol{G}}^{S}$ and $V_{\boldsymbol{G}}^{A}$ are the symmetric and anti-symmetric components of the pseudopotential form factors, respectively, and are given by

$$V_{\boldsymbol{G}}^{S} = \frac{1}{\Omega}\int \left(V_a(\boldsymbol{r}) + V_b(\boldsymbol{r})\right)e^{i(\boldsymbol{G}'-\boldsymbol{G})\cdot\boldsymbol{r}}\, d\boldsymbol{r} \qquad (3.9)$$

and

$$V_{\boldsymbol{G}}^{A} = \frac{1}{\Omega}\int \left(V_a(\boldsymbol{r}) - V_b(\boldsymbol{r})\right)e^{i(\boldsymbol{G}'-\boldsymbol{G})\cdot\boldsymbol{r}}\, d\boldsymbol{r} \qquad (3.10).$$

From the analysis of Fig. 3.2b, the terms involving the positions of the atoms can be expressed using

$$\boldsymbol{v} = \frac{c}{4}\hat{\boldsymbol{z}} \tag{3.11},$$

$$\boldsymbol{h}_B = \frac{a}{2}\hat{\boldsymbol{x}} + \frac{a}{2\sqrt{3}}\hat{\boldsymbol{y}} \tag{3.12},$$

and

$$\boldsymbol{h}_C = \frac{a}{\sqrt{3}}\hat{\boldsymbol{y}} \tag{3.13}$$

where $\boldsymbol{v}$ is the separation between each layer, and $\boldsymbol{h}_B$ and $\boldsymbol{h}_C$ are the location of the B layer and C layer lattices sites in the *xy*-plane, respectively. Using these definitions, the crystal pseudopotential can be written as

$$V_{\boldsymbol{G},\boldsymbol{G}'} = \left[V_{\boldsymbol{G}}^{S}\, cos\big((\boldsymbol{G}' - \boldsymbol{G})\cdot\boldsymbol{s}\big) + iV_{\boldsymbol{G}}^{A}\, sin\big((\boldsymbol{G}' - \boldsymbol{G})\cdot\boldsymbol{s}\big)\right]$$

$$\times\left[1 + e^{-i(\boldsymbol{G}'-\boldsymbol{G})\cdot(\boldsymbol{v}+\boldsymbol{h}_B)} + e^{-i(\boldsymbol{G}'-\boldsymbol{G})\cdot(2\boldsymbol{v}+\boldsymbol{h}_C)} + e^{-i(\boldsymbol{G}'-\boldsymbol{G})\cdot(3\boldsymbol{v}+\boldsymbol{h}_B)}\right] \tag{3.14}$$

The calculation of the band structure can proceed, once the pseudopotential form factors $V_{\boldsymbol{G}}^{S}$ and $V_{\boldsymbol{G}}^{A}$ are known. The approach taken to finding the pseudopotential form factors will be to use them as adjustable parameters to fit known energy band gaps and effectivemasses. This will be done through the use of a genetic algorithm approach, detailed in the next section.

3.4. Genetic Algorithm Fitting

Genetic algorithms (GA) have been utilized in a variety of disciplines to optimize parameters of multi-dimensional functions. Within the area of band structure calculations, GA's were first demonstrated by Starrost *et al.* as being effective in

adjusting up to eleven tight-binding parameters to fit the energy band gaps of various zinc-blende semiconductors [20]. Klimeck *et al.* have also used GA's to adjust up to 20 parameters in a second-nearest neighbor tight-binding model to fit effective masses as well as band gap energies [21]. In addition, genetic algorithms have been employed in inverse band structure calculations to find atomic configurations and lattice constants in order to engineer materials with a given band structure [22,23]. Genetic algorithms have thus been shown to be effective at providing an automated way to search for and to optimize tight-binding calculations with an arbitrary number of parameters. Here it will be shown that this strategy can be equally as effective in finding band structure parameters for an EPM calculation.

The strategy of a GA is very similar to evolutionary processes in the real world. The optimization proceeds by first randomly generating a population of possible solutions. The parameters of the problem are identified as the "genes" that make up a solution. Each of the possible solutions is evaluated according to a pre-defined weighting scheme. The most "fit" of the solutions are chosen to survive and kept within the population, while the underperforming solutions are discarded. The population is then replenished by having the fittest solutions "reproduce" – they create new solutions in a process called "crossover" by randomly taking parameters from two existing fit solutions. In order to create solutions with parameters having values not previously existing in the original population, genes may randomly "mutate" to take on new values. The cycle is repeated until the solutions converge or a preset number of iterations have been performed. From the preceding description, it is clear that the GA has four steps: initialization of the original population, selection of solutions based upon a fitness evaluation, reproduction through crossover and mutation to create new solutions, and termination of the process after some criterion is met. As is obvious, the algorithm is largely stochastic.

Nevertheless, GA's have been frequently observed to successfully produce reasonable solutions. A flowchart of this algorithm is shown in Fig. 3.3.

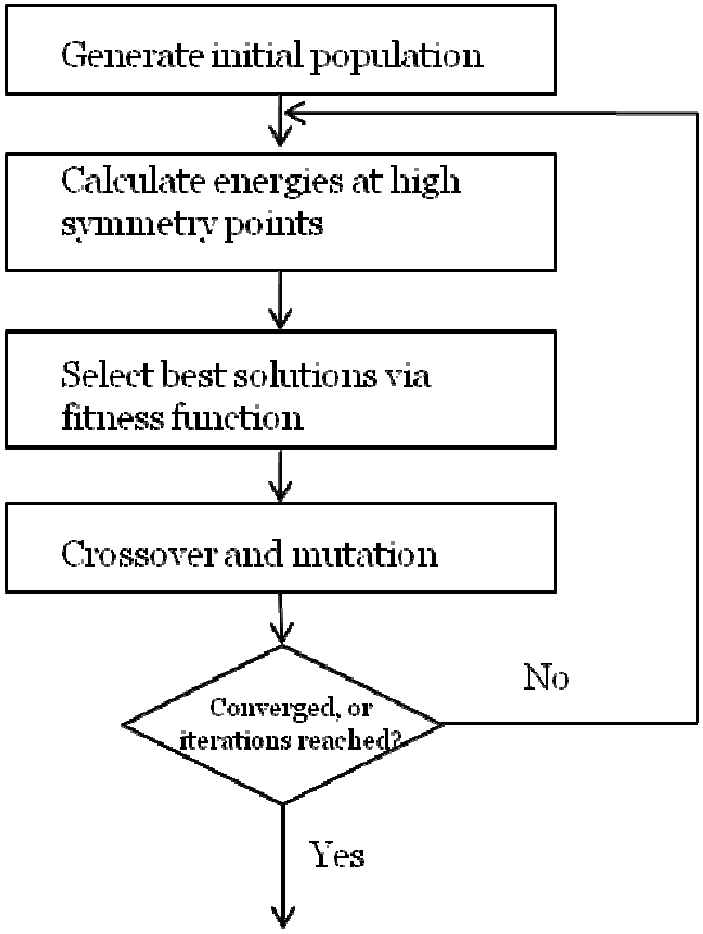

Fig. 3.3. Flowchart of the genetic algorithm.

The first step of the GA proceeds by initializing the parameters of the original population. The style in which the parameters are encoded must first be chosen. There are two options on how this can be done. One method is to convert all the parameter values into binary strings and then merge them all into a single, long chromosome. The other approach is to treat each of the parameters as "genes," keeping their real values

which are then passed along when creating new solutions. The set of parameters is then considered as the chromosome. Each approach has trade-offs to be considered. For example, encoding parameters into binary strings allows a more straight forward manipulation during the crossover operation, while keeping parameters as real values allows one to control the range that the parameters can take on to avoid unphysical results [19].

In the selection step, each of the possible solutions is evaluated through an objective function. The objective function for band structure fitting usually takes the form of

$$d(\boldsymbol{m}) = -\left(\frac{1}{\sum_n w_n}\left[\sum_{n'} w_{n'}\left(E_{n'}(\boldsymbol{m}) - E_{n',tar}\right)^2\right]\right)^{1/2} \tag{3.15}$$

where $d(\boldsymbol{m})$ is the fitness of a solution calculated with the set of parameters $\boldsymbol{m}$, $E_n(\boldsymbol{m})$ are the energies calculated with the set of parameters $\boldsymbol{m}$, $E_{n,tar}$ is the targeted goal value for energy n, and w_n is a weight chosen from an interval [1,100] based on the importance of that energy [20]. The difference between the calculated energy and the targeted value is squared to penalize larger deviations from the goal values. The negative sign in front Eq. (3.15) drives the GA to maximize $d(\boldsymbol{m})$; however, the GA can just as well become a minimization problem by removing the negative sign. Hard minimum or maximum values for particularly important energies can also be included by setting Eq. (3.8) to an arbitrarily low value if the calculated energy falls out of an acceptable range [21].

The crossover and mutation step is performed after selection of the fittest solutions. How the crossover and mutation steps are implemented is largely based upon how the parameters are encoded in the initialization. For binary coded parameters different segments of the binary string chromosomes of the two parents are combined in the crossover step, while the mutation operator will with a given probability reverse one or more of the bits in the binary string. For real valued encoding, each gene of the child

randomly inherited from one of the two parents. The mutation operator will change these values, subject to a user specified range. Vitally important for either encoding is the probability of mutation. Generally it has been observed that lower mutation rates give faster convergence, while higher mutation rates take longer to converge but give better results. Alternatively, a variable mutation rate can be implemented so that the more similar two parents are, the higher the mutation rate becomes.

The termination of the GA is largely arbitrary. Since absolute convergence will normally not be achieved, often the termination condition will be after a given number of iterations. Another criterion that can be used is when the energy values to be fitted reach an acceptable accuracy. The GA can then be programmed to terminate once the energies are within some tolerance level.

3.5. Results of the Genetic Algorithm Fitting of 4H SiC

Using the crystal pseudopotential expression and genetic algorithm fitting procedure of the preceding two sections, the electronic band structure of 4H SiC was calculated. For the material parameters, the lattice constants $a = 3.032\,\text{Å}$ and $c = 9.928\,\text{Å}$, and bond length $L_z = 1.866\,\text{Å}$ were used. These parameters were taken from the theoretical work of Kackell *et al*. who arrived at them by finding the values that minimized the total energy [24]. A total of 575 plane waves for a cutoff energy of 205 eV was used since this lies in a range has been observed to give good convergence results in diamond and zinc-blende materials [25]. For the Fourier coefficients, which act as the adjustable parameters used in the calculation, 19 distinct symmetric and anti-symmetric components were included. The GA sought solutions by varying these form factors from a range of -0.25 Ry to 0.25 Ry, discretized to units of 0.001 Ry.

In terms of the GA, all the published experimental electronic structure data were targeted by the fitting procedure. These experimental data include: the indirect Γ to M

band gap energy, the direct energy transitions at the Γ, M, K and L points, the energy difference between the first and second conduction band energies at the M point, and the total valence band energy. The split-off energy at the top of the valence band was also included, although this cannot be completely and properly accounted for without including spin-orbit interaction effects. In addition, the direct energy gaps at the A and H points deduced from *ab initio* calculations by Wenzien *et al.* and Baumeier *et al.* were included as additional fitting targets. The choice of weights for each of these criterion were arrived at by assigning all experimental energy gaps with a weight of 100, while the energy gaps predicted by the *ab initio* calculations were assigned a weight of 70. The weight for the total valence band energy, however, was given a value of 20 since its target value is much larger than the other criterion. Deviations from this value would count disproportionately if it was weighted the same as the other energies. Also, the weight for the split-off energy was assigned a weight of 70 since it cannot be completely accounted for in this approach.

An initial population of 200 solutions was used, with half the population replaced after each iteration. For the gene encoding, a real-valued scheme was used since large number of EPM form factors lends itself to this approach. Each pseudopotential form factor is therefore treated as a gene, and child solutions inherit these randomly from one of two parent solutions. A variable mutation probability was employed, varying linearly from about 6% for two solutions with no complementary form factors in common to about 17% for two duplicate solutions. An illustration of the crossover and mutation operations of the reproduction step is illustrated in Fig. 3.4.

In total, the genetic algorithm was run for 250 iterations before being terminated. The resultant band structure is plotted along several high symmetry points of the hexagonal structure in Fig. 3.5, while the form factors are given in Table I. The fit

arrived at by the genetic algorithm is very satisfactory compared to the experimental values. The band gap energy arrived at is 3.28 eV, while the direct Γ, M, K and L energy transitions obtained are 6.30, 4.42, 7.90 and 6.03 eV, respectively. The total valence band is 19.25 eV wide. Comparatively, the EPM calculation by Zubkova *et al.* give a band gap energy smaller by about 0.3 eV, a direct Γ transition smaller by 1.6 eV and a direct L transition smaller by more than 1.5 eV. The EPM calculation by Pennington *et al.* underestimates the direct Γ transition by more than 1 eV and overestimates the direct M transition by about the same energy. At the same time, the calculation has been simplified by requiring 12 less fitting parameters.

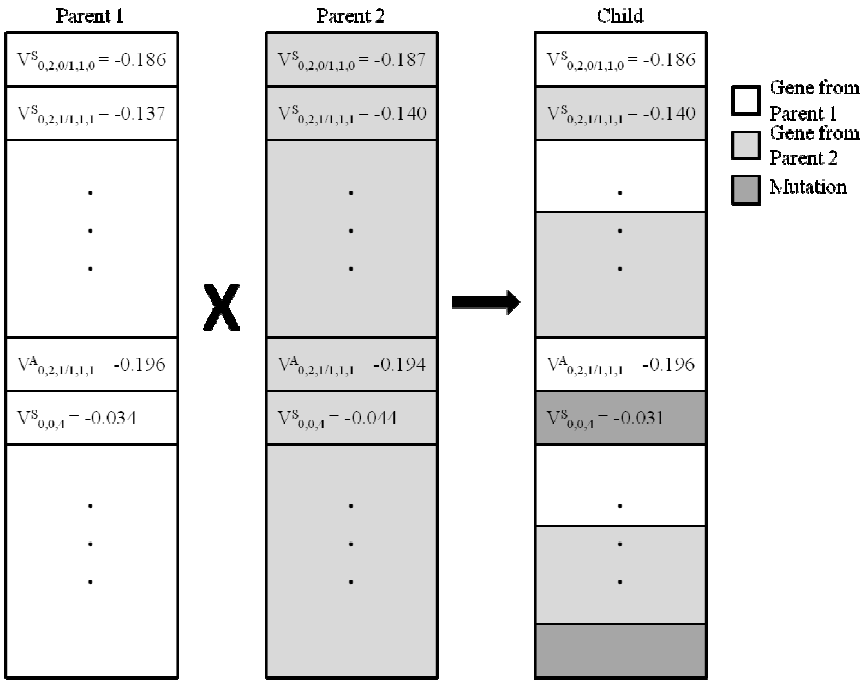

Fig. 3.4. Illustration of the real-valued parameter encoding, and the crossover and mutation operations in the reproduction step. Each of the parameters is interpreted as a "gene," with each gene of the child either inherited from a random parent or being a new value generated by mutation.

Using this band structure, the electron effective masses along the the M-Γ, M-L and M-K directions were calculated. As shown in Fig. 3.6, this was done by fitting a parabola to the lowest 0.05 eV portion of the conduction band minimum, where the majority of electrons reside at room temperature, using a least squares fit. The values of the effective masses obtained are $m^*_{M\Gamma} = 0.66m_0$, $m^*_{M\mathrm{K}} = 0.31m_0$, $m^*_{M\mathrm{L}} = 0.34m_0$ which are in good agreement with the experimentally measured values of $m^*_{M\Gamma} = 0.58m_0$, $m^*_{M\mathrm{K}} = 0.29m_0$, $m^*_{M\mathrm{L}} = 0.33m_0$ [26]. Table II shows a comparison between the values of the energy transitions and effective masses obtained from this study and previous experimental measurements.

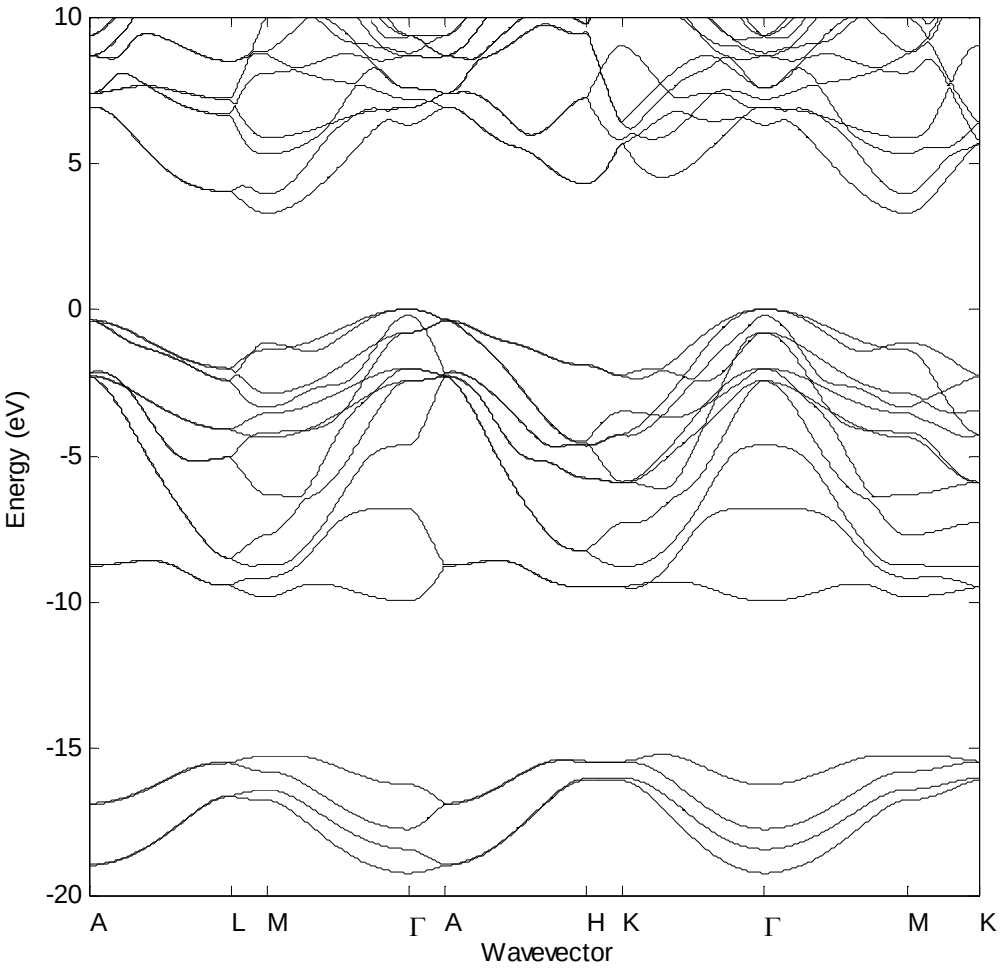

Fig. 3.5. Band structure for 4H SiC using 575 plane waves.

Table 3.1. EPM form factors for 4H SiC in Rydbergs determined by the GA, grouped together by reciprocal lattice vectors with the same magnitude, where k_x is scaled by $a/2\pi$, k_y is scaled by $a\sqrt{3}/2\pi$, and k_x is scaled by $a/2\pi$, k_z is scaled by $c/2\pi$. Not included are form factors for which the reciprocal lattice vectors cause the structure factor to vanish.

G	V^S	V^A
(0,2,0) (1,1,0)	-0.186	
(0,2,1) (1,1,1)	-0.140	-0.196
(0,0,4)	0.103	-0.031
(0,2,2) (1,1,2)	-0.111	-0.034
(0,2,3) (1,1,3)	-0.022	-0.007
(0,2,4) (1,1,4)	-0.107	-0.094
(0,2,5) (1,1,5)	-0.034	-0.058
(2,0,0) (1,3,0)	0.085	
(0,2,6) (1,1,6)	0.041	-0.124
(0,4,0) (2,2,0)	0.004	
(0,4,1) (2,2,1)	0.007	0.003

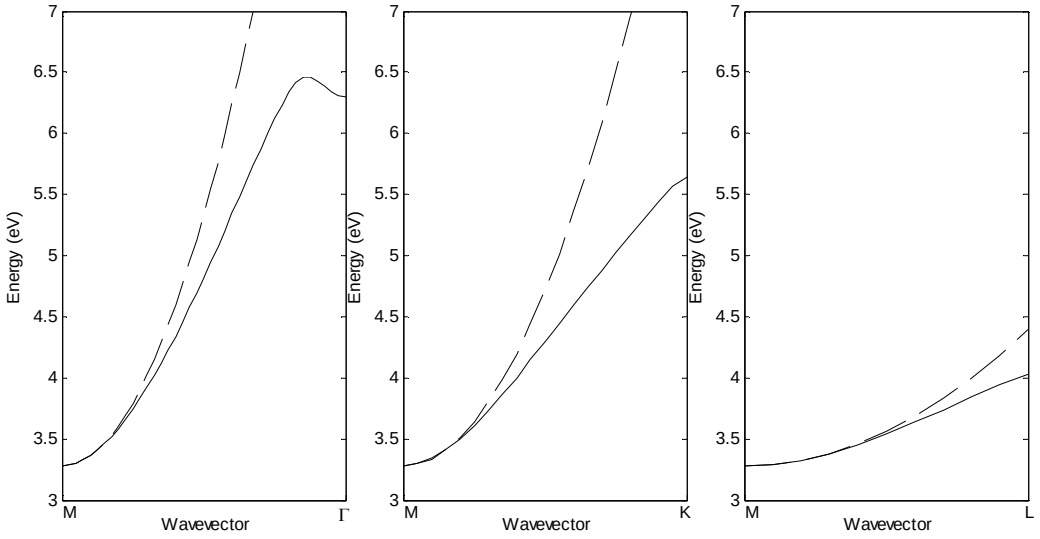

Fig. 3.6. Shape of the calculated (−) lowest conduction band along the M-Γ, M-K and M-L directions, fitted with a least square parabolic approximation (--).

Table 3.2. Energy transitions of the indirect and the direct band gap at high symmetry points Γ, *M*, *K* and *L*, and effective masses of 4H SiC calculated in this work compared to experimental results. The energy transitions are in eV, while the effective masses are in units of m_0.

	Energy Transitions					Effective Masses		
	E_g	Γ	*M*	*K*	*L*	$m_{M\Gamma}$	m_{MK}	m_{ML}
Expt.	3.26[a]	6.18[b],6.2[c]	4[c],4.5[b]	7.8[c]	6.7[c]	0.58[d]	0.29[d]	0.33[d]
This Work	3.28	6.30	4.42	7.9	6.03	0.66	0.31	0.34

[a] Reference 16.
[b] Reference 18.
[c] Reference 17.
[d] Reference 26.

CHAPTER 4. QUANTUM SCATTERING THEORY

4.1. Introduction

Using the properties from the electronic band structure, further quantities such as transport properties can be calculated. The band structure is necessary because transport in bulk semiconductors is treated semi-classically. In essence, this means that the influence of the crystal potential on carriers is treated through an effective mass or, if more accuracy is needed, the full band structure. In every other respect, carriers are treated classically as particles that obey Newton's laws in response to applied and built in potentials [27].

In this chapter, the foundations needed to make these transport calculations will be presented. First, Fermi's Golden rule will be discussed, and the definitions of the various characteristic rates are given. The derivations will largely follow those given by Lundstrom [27]. These results summarize the effects of all scattering mechanisms. Subsequently, the characteristic rates for specific scattering mechanisms important to SiC are derived.

4.2. Fermi's Golden Rule

As discussed in the previous chapter, electrons in a solid can be thought of as Bloch waves that move through the crystal potential. However, in real materials, these waves frequently encounter perturbing potentials – either from impurities or from phonons – causing them to be scattered and their momentums to be relaxed. The quantity that describes this scattering is called the scattering rate, $S_{\boldsymbol{k},\boldsymbol{k}'}$. This is the long-time average probability that an electron with wave vector $\boldsymbol{k}$ will, after interacting with a perturbing potential, emerge with a wave vector $\boldsymbol{k}'$.

To obtain the general expression for the scattering rate, the Schrödinger equation of an electron in the presence of a scattering potential must be solved. Assuming the

problem is one-dimensional for simplicity, the Schrödinger equation is in the form of

$$\big(H_0 + U_S(x,t)\big)\Psi(x,t) = i\hbar\frac{\partial\Psi(x,t)}{\partial t} \tag{4.1}$$

where H_0 is the Hamiltonian for the unperturbed problem, $U_S(x,t)$ is the scattering potential, and $\Psi(x,t)$ is the wave function of the electron. Furthermore, it is assumed that the solutions to the unperturbed problem is known so that

$$\Psi_k^0(x,t) = \psi_k(x)e^{-iE_kt/\hbar} \tag{4.2}$$

where ψ_k is an eigenfunction of H_0 with corresponding eigenvalue E_k, and Ψ_k^0 is the corresponding time-dependant solution. From basic quantum mechanics, it is known that the ψ_k's form a complete orthonormal set. Consequently, any wave function of the perturbed potential in Eq. (4.1) can be expanded as

$$\Psi(x,t) = \sum_k c_k(t)\Psi_k^0(x,t) = \sum_k c_k(t)\psi_k(x)e^{-iE_kt/\hbar} \tag{4.3}$$

where $c_k(t)$ is the expansion coefficient for each eigenstate ψ_k. These expansion coefficients are interpreted in quantum mechanics as being related to the long-time probability that an electron is in a state k, given by the expression

$$P_k = \lim_{t\to\infty}|c_k(t)|^2 \tag{4.4}.$$

The scattering rate from k to k' is then

$$S_{k,k'} = \lim_{t\to\infty}\frac{|c_k(t)|^2}{t} \tag{4.5}$$

The form of the c_k's can be found by exploiting the orthogonality of Eq. (4.2). The wave function of Eq. (4.3) is inserted into Eq. (4.1) resulting in

$$U_S(x,t)\sum_k c_k(t)\psi_k(x)e^{-iE_kt/\hbar} = i\hbar\sum_k \frac{\partial c_k}{\partial t}\psi_k(x)e^{-iE_kt/\hbar} \qquad (4.6).$$

Multiplying each side by $\psi_k^* e^{iE_kt/\hbar}$ and integrating over the normalization length results in

$$i\hbar\frac{\partial c_k}{\partial t} = \sum_k H_{k',k}c_k(t)e^{i(E_{k'}-E_k)t/\hbar} \qquad (4.7)$$

where

$$H_{k',k}(t) = \int_{-L/2}^{L/2}\psi_{k'}(x)U_S(x,t)\psi_k(x)dx \qquad (4.8)$$

is called the matrix element of the scattering potential. To proceed any further, an assumption must be made. The scattering in the problem is taken to be weak and infrequent so that the probability of an electron in an arbitrary state k_0 is $c_{k_0} \approx 1$, and all other probabilities are $c_k \approx 0$. This is known as the Born approximation and results in only one term in Eq. (4.6) surviving, giving

$$i\hbar\frac{\partial c_{k_0'}}{\partial t} = H_{k_0'k_0}e^{i\left[E_{k_0'}-E_{k_0}\right]t/\hbar} \qquad (4.9).$$

Integrating Eq. (4.8) results in the expression for $c_{k_0'}(t)$,

$$c_{k_0'} = \frac{1}{i\hbar}\int_0^t H_{k_0'k_0}e^{i\left[E_{k_0'}-E_{k_0}\right]t/\hbar}dt \qquad (4.10)$$

which includes a constant equal to $c_{k_0'}(0)$. However, in accordance with the Born approximation, the probabilities for all states other than k_0 before the scattering event is approximately zero.

To arrive at a final expression for $S_{\boldsymbol{k},\boldsymbol{k'}}$, the time-dependent matrix elements is assumed to have a time harmonic form of

$$H_{k_0',k_0}(t) = H_{k_0',k_0}^{a,e} e^{\mp i\omega t} \tag{4.11},$$

where the a stands for absorption and the e stands for emission. Inserting Eq. (4.10) into Eq. (4.9) and integrating results in

$$c_{k_0'} = \frac{1}{i\hbar} H_{k_0',k_0}^{a,e} \frac{e^{i\left(E_{k_0'} - E_{k_0} \mp \hbar\omega\right)t/\hbar} - 1}{i\left(E_{k_0'} - E_{k_0} \mp \hbar\omega\right)/\hbar} \tag{4.12}.$$

By defining

$$\Lambda = i\left(E_{k_0'} - E_{k_0} \mp \hbar\omega\right)/\hbar \tag{4.13}$$

Eq. (4.11) can be written in a more compact form given by

$$c_{k_0'} = \frac{1}{i\hbar} H_{k_0',k_0}^{a,e} e^{i\Lambda t/2} \frac{\sin(\Lambda t/2)}{\Lambda t/2} t \tag{4.14}.$$

Using Eq. (4.11) the resulting transition rate is

$$S_{k_0,k_0'} = \lim_{t\to\infty} \frac{\left|H_{k_0',k_0}^{a,e}\right|^2}{t\hbar^2} \left[\frac{\sin(\Lambda t/2)}{\Lambda t/2}\right]^2 t^2 \tag{4.15}.$$

In the limit of $t \to \infty$, the sinc function approaches a delta function with a strength of π. With this substitution the resulting expression is

$$S_{k_0,k_0'} = \lim_{t\to\infty} \frac{\left|H_{k_0',k_0}^{a,e}\right|^2}{t\hbar^2} \left[\frac{\sin(\Lambda t/2)}{\Lambda t/2}\right]^2 t^2$$

$$= \lim_{t\to\infty} \frac{\pi\left|H_{k_0',k_0}^{a,e}\right|^2}{\hbar^2} \delta(\Lambda t/2) t = \lim_{t\to\infty} \frac{\pi\left|H_{k_0',k_0}^{a,e}\right|^2}{\hbar^2} \delta(\Lambda)\left(\frac{2}{t}\right) t$$

$$= \frac{2\pi}{\hbar}\left|H_{k_0',k_0}^{a}\right|^2 \delta\left(E_{k_0'} - E_{k_0} - \hbar\omega\right)$$

$$+ \frac{2\pi}{\hbar}\left|H_{k_0',k_0}^{e}\right|^2 \delta\left(E_{k_0'} - E_{k_0} + \hbar\omega\right) \tag{4.16}.$$

The correspondence between the absorption and the emission matrix elements to each delta function results because in absorption the final state's energy is $E_{k_0'} = E_{k_0} + \hbar\omega$, while in emission the final state's energy is $E_{k_0'} = E_{k_0} - \hbar\omega$. This result in scattering theory is known as Fermi's Golden Rule, and it allows one to calculate the transition rate of any scattering process if one knows the corresponding scattering potential.

Once the transition rate is known, a set of characteristic rates can be derived that concisely summarize the effects of scattering mechanisms in a semiconductor. One of these is the scattering rate, defined as the rate carriers scatter out of an initial wave vector (or momentum) into any other wave vector (momentum). This is calculated as

$$\frac{1}{\tau} = \sum_{\boldsymbol{p}',\uparrow} S_{\boldsymbol{p},\boldsymbol{p}'}\left[1 - f_{\boldsymbol{p}'}\right] \approx \sum_{\boldsymbol{p}',\uparrow} S_{\boldsymbol{p},\boldsymbol{p}'} \tag{4.17}$$

where instead of using the wave vector the crystal momentum $\boldsymbol{p} = \hbar\boldsymbol{k}$ is used instead. The approximation in Eq. (4.17) can be made for non-degenerate semiconductors, since in these cases the probability for the final momentum state to be occupied is low.

Another important characteristic rate is the momentum relaxation rate. This is the rate at which an electron loses information in the direction of its initial momentum. The expression relating the transition rate to the momentum relaxation rate is found by weighting the transition rate by the change in direction of the carriers,

$$\frac{1}{\tau_m} = \sum_{\boldsymbol{p}',\uparrow} S_{\boldsymbol{p},\boldsymbol{p}'}\left[1 - \left(\frac{p'}{p}\right)\cos\alpha\right] \tag{4.18}$$

where α is the angle between the initial and final momenta (see Fig. 4.1), while the up arrow in the summation indicates the inclusion of only the final momenta with a spin parallel to the initial momentum. An important result to note is that when the transition rate is isotropic, the relaxation rate and momentum relaxation rate are equal for non-degenerate semiconductors.

Finally, the last characteristic time of interest is the energy relaxation time. In contrast to the momentum relaxation time, this is the rate at which the magnitude of the momentum (which is a measure of energy) is randomized. In a similar manner to the momentum relaxation rate, this is found by weighting the transition rate by the change in the energy of the carriers,

$$\frac{1}{\tau_m} = \sum_{\boldsymbol{p}',\uparrow} S_{\boldsymbol{p},\boldsymbol{p}'} \left[1 - \frac{E_{p'}}{E_p}\right] \tag{4.19}.$$

The various relaxation times are illustrated in Fig. 4.1b.

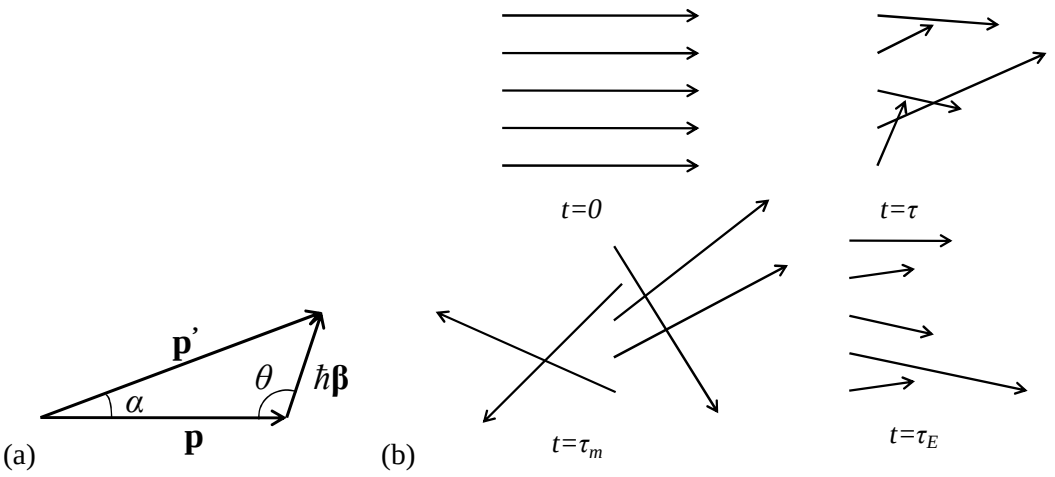

Fig. 4.1. (a) The momentum, final momentum, and emitted/absorbed phonon vectors with the various angles defined between them. (b) Illustration of the various characteristic times.

The rest of this remaining chapter will focus in detail on each of the scattering mechanisms important in SiC. Emphasis will be placed on deriving the relaxation rate and the momentum relaxation rate, since it is these quantities that are of interest in calculating mobility.

4.3. Scattering Mechanisms and Momentum Relaxation Rates

Once the scattering potential is known, and using Fermi's Golden Rule, any of the characteristic rates can be calculated. This section provides a brief overview of the characteristic rates important to SiC; however, no detailed derivation of them will be given. The scattering potentials for each mechanism will be assumed to be known, and mathematical details of the summations (integrals) of the form of Eq. (4.17) and Eq. (4.18) will be largely omitted. However, mathematically rigorous derivations are covered thoroughly in the literature [27-29].

The scattering mechanisms under consideration can be classified into many broad categories. One division is between impurity scattering due to atoms different from the host atoms of the material and phonon scattering due to lattice vibrations. Phonon scattering can further be subdivided according to whether it is non-polar (single element semiconductors) or polar (compound semiconductors) scattering. Each of these preceding categories can further be subdivided according to whether the scattering is by acoustic or optical phonons. Each of these will be covered in the subsequent sections.

4.3.1. Ionized Impurity Scattering

Several theories have been developed to describe electron scattering by ionized impurities. One approach, valid for degenerate systems, was developed by Mott and is suitable for impure metallic systems [30]. For semiconductors, one widely used approach is the theory developed by Brooks and Herring, which assumes ionized impurities attract mobile carriers which screen their potential [27-29]. A drawback to this approach is that it predicts an infinite scattering probability for small angle deflections when the screening is low. This is remedied by an approach developed by Conwell and Weisskopf, whose theory assumes no screening but avoids the divergent scattering probabilities [31]. However, the assumption of unscreened Coulomb scattering for small angles is known to

be not very accurate, and therefore this section will focus on the formulation of Brooks and Herring.

The perturbing potential in this case is due to donor or acceptor atoms in the host material that become ionized, and is screened by the free carrier concentration. This potential has the form of a Yukawa potential,

$$U_S(r) = \frac{q^2}{4\pi\kappa_S\varepsilon_0 r} e^{-r/L_D} \tag{4.20}$$

where κ_S is the dielectric constant of the material and r is the distance from the impurity. The quantity L_D is known as the Debye length, and is given by

$$L_D = \sqrt{\frac{\kappa_S\varepsilon_0 k_B T}{q^2 N_I}} \tag{4.21}$$

where k_B is the Boltzmann constant, T is the temperature and N_I is the number of ionized impurities in the sample. Using Eq. (4.20) in Eq. (4.8) with Bloch waves as the form of the solutions ψ_k and integrating results in

$$H_{\boldsymbol{p}',\boldsymbol{p}} = \frac{q^2}{\Omega\kappa_S\varepsilon_0} \frac{1}{p^2 \sin^2\left(\frac{\alpha}{2}\right) + \left(\frac{1}{L_D^2}\right)} \tag{4.22}.$$

where Ω is the normalization volume and α is the angle between the incident and scattered momenta. Inserting Eq. (4.22) into Eq. (4.16) and multiplying by the number of impurities in the normalization volume, $N_I\Omega$, gives the expression for the ionized impurity transition rate

$$S_{\boldsymbol{p},\boldsymbol{p}'} = \frac{2\pi N_I q^4}{\hbar\kappa_S^2\varepsilon_0^2\Omega} \frac{\delta(E'-E)}{\left[4\left(\frac{p}{\hbar}\right)^2 \sin^2\left(\frac{\alpha}{2}\right) + \left(\frac{1}{L_D^2}\right)\right]^2} \tag{4.23}.$$

As briefly mentioned earlier, the scattering potential of Eq. (4.20) is obtained by assuming ionized impurities are screened by mobile carriers. When a region is absent of mobile carriers, such as in a depletion region in a device, $L_D \to \infty$ and the second term in

the denominator of Eq. (4.23) vanishes. As the angle of deflection approaches zero, this would result in a divergent scattering rate. In these cases, either a lower limit to the scattering angle must be provided, or another approach such as the Conwell-Weisskopf approximation, must be used.

Finally, the momentum relaxation rate is obtained by substituting Eq. (4.23) into Eq. (4.18) and integrating over all final states producing

$$\frac{1}{\tau_{m,ii}} = \frac{N_I q^4}{16\sqrt{2m^*}\pi\kappa_s^2\varepsilon_0^2 E_k^{3/2}}\left[ln(1+\gamma^2) - \frac{\gamma^2}{1+\gamma^2}\right] \tag{4.24}$$

where $\gamma^2 = 8m^* E_k L_D^2/\hbar^2$.

4.3.2. Neutral Impurity Scattering

Another category of impurity scattering is due to non-ionized shallow donors and acceptors, and contributes significantly to the total scattering rate if the doping concentration is high and the temperature is low [29]. This is known as neutral impurity scattering, and was first treated theoretically as slow electrons colliding with a neutral hydrogen atom. This approach was first developed by Massey and Moisewitch [32], and later extended to impurities in semiconductors by Erginsoy [33]. The resulting momentum relaxation rate is constant with respect to energy and is given by

$$\frac{1}{\tau_{m,ni}} = \frac{80\pi\kappa_s\varepsilon_0\hbar^3 N_n}{e^2 m^{*2}} \tag{4.25}$$

where N_n is the number of neutral impurities present.

Many other alternative formulations to Erginsoy's exist. One such approach is that due to Sclar [34], who treated the scattering by neutral impurities as due to a spherically symmetric square-well potential which can bind an electron to it. The resulting momentum relaxation rate using this approach is

$$\frac{1}{\tau_{m,ni}} = \frac{2^{3/2}\pi\hbar^2 N_n}{m^{*3/2}}\left(\frac{E_k^{1/2}}{E_k + E_T}\right) \tag{4.26}$$

where $E_T = 0.75\frac{m^*}{m}\left(\frac{1}{\kappa_s}\right)^2$ eV is the binding energy for a second electron on a hydrogen atom. It is clear that with Sclar's formula larger binding energies would result in longer momentum relaxation times. Thus, deep levels which bind electrons do not act as strong scattering centers.

4.3.3. Scattering and Relaxation Rates for Phonons

In addition to impurities, the other major class of scattering centers in semiconductors is due to phonons. The perturbing potential in this case is from pressure that changes the lattice constants. In compound semiconductors, an additional interaction arises due to the polar nature of the bonds. On this basis, the scattering can be divided into two categories: non-polar and polar. In addition, since the phonon dispersion curves exhibit two branches – acoustic modes that propagate in a manner similar to sound waves and optical modes interact with light – each scattering mechanism can further be divided into two more categories. This results in four different scattering mechanisms: acoustic deformation potential (ADP), optical deformation potential (ODP), polar acoustic deformation potential (also known as piezoelectric, PZ), and polar optical potential (POP).

The scattering potentials for each of these mechanisms can be written in general as

$$U_S = K_\beta u_\beta \tag{4.27}.$$

In this equation u_β is of the form of an one dimensional elastic wave with wave vector β and is given by

$$u_\beta(x,t) = A_\beta e^{i(\beta x - \omega t)} + A_\beta^* e^{-i(\beta x - \omega t)} \tag{4.28}$$

where A_β is the magnitude of displacement. The factor K_β depends on the scattering mechanism, and its magnitude squared for each of the four different mechanisms is given by

$$\left|K_\beta\right|^2 = \beta^2 D_A^2 \text{ (DP)} \tag{4.29},$$

$$\left|K_\beta\right|^2 = D_o^2 \text{ (ODP)} \tag{4.30},$$

$$\left|K_\beta\right|^2 = \left(\frac{\rho q^2 \omega_o^2}{\beta^2 \kappa_0 \varepsilon_0}\right)\left(\frac{\kappa_0}{\kappa_\infty} - 1\right) \text{ (POP)} \tag{4.31},$$

$$\left|K_\beta\right|^2 = \left(\frac{q e_{PZ}}{\kappa_0 \varepsilon_0}\right)^2 \text{ (PZ)} \tag{4.32},$$

where D_A is the acoustic deformation potential, D_o is the optical deformation potential, ω_o is related to the polar optical phonon energy, κ_∞ is the high frequency dielectric constant, and e_{PZ} is the piezoelectric constant. The deformation potentials and polar optical phonon energies are usually determined experimentally, while the piezoelectric constant is related to electromechanical coupling coefficient which can be determined by the elastic constants of the material.

Using Eq. (4.27), a general expression for the scattering matrix element of phonons can be written as

$$\left|H_{\boldsymbol{p}',\boldsymbol{p}}\right|^2 = \left|K_\beta\right|^2 \left|A_\beta\right|^2 \delta_{\boldsymbol{p}',\boldsymbol{p}\pm\hbar\boldsymbol{\beta}} \tag{4.33}.$$

Directly inserting this result into Fermi's Golden Rule in Eq. (4.16) and assuming parabolic energy bands gives the general transition rate for phonon scattering processes,

$$S_{\boldsymbol{p}',\boldsymbol{p}} = \frac{2\pi}{\hbar}\left|K_\beta\right|^2 \left|A_\beta\right|^2 \delta_{\boldsymbol{p}',\boldsymbol{p}\pm\hbar\boldsymbol{\beta}} \delta\left(E' - E \mp \hbar\omega_\beta\right) \tag{4.34}.$$

Each of the delta functions expresses a conservation law (momentum and energy, respectively), and in order to evaluate their product the energy will need to be expressed in terms of momentum. This is done by first noting that the Kronecker delta function indicates that the final, scattered momentum is just the initial momentum that has absorbed or emitted additional momentum due to phonons,

$$\boldsymbol{p}' = \boldsymbol{p} \pm \hbar\boldsymbol{\beta} \tag{4.35}.$$

Taking the dot product of the final momentum with itself results in

$$\boldsymbol{p}' \cdot \boldsymbol{p}' = p^2 \pm 2\hbar p\beta\cos\theta + \hbar^2\beta^2 \tag{4.36}$$

where θ is the angle between $\boldsymbol{p}$ and $\boldsymbol{\beta}$ (see Fig. 4.1a). With the assumption of parabolic energy bands and using substituting velocity for momentum in Eq. (4.36) results in

$$E' - E \mp \hbar\omega_\beta = \hbar\upsilon\beta\left(\pm\cos\theta + \frac{\hbar\beta}{2p} \mp \frac{\omega_\beta}{\upsilon\beta}\right) \tag{4.37}.$$

Since Eq. (4.37) includes the constraint of conservation of momentum in the energy expression, the transition rate can be written with just one delta function as

$$S_{\boldsymbol{p}',\boldsymbol{p}} = \frac{2\pi}{\hbar^2\upsilon\beta}\left|K_\beta\right|^2\left|A_\beta\right|^2\delta\left(\pm\cos\theta + \frac{\hbar\beta}{2p} \mp \frac{\omega_\beta}{\upsilon\beta}\right) \tag{4.38}.$$

The magnitude squared of the lattice vibration is determined by taking into account quantum mechanical considerations. Phonon scattering events result from either absorbing or emitting quantized lattice vibrations, and this is expressed in the form

$$\left|A_\beta\right|^2 = \frac{\hbar}{2\rho\Omega\omega_\beta}\left(N_\beta + \frac{1}{2} \mp \frac{1}{2}\right) \tag{4.39}$$

where N_β is the number of phonons determined by the Bose-Einstein distribution, and the minus (plus) sign is for phonon absorption (emission). Substituting Eq. (4.39) into Eq. (4.38) gives the general transition rate for phonons,

$$S_{\boldsymbol{p}',\boldsymbol{p}} = C_\beta \left(N_\beta + \frac{1}{2} \mp \frac{1}{2}\right) \delta\left(\pm \cos\theta + \frac{\hbar\beta}{2p} \mp \frac{\omega_\beta}{\upsilon\beta}\right) \tag{4.40}$$

with C_β being determined by the scattering process,

$$C_\beta = \frac{\pi m^* D_A^2}{\hbar \rho \upsilon_S p \Omega} \text{ (DP)} \tag{4.41},$$

$$C_\beta = \frac{\pi m^* D_o^2}{\hbar \rho \omega_0 \beta p \Omega} \text{ (ODP)} \tag{4.42},$$

$$C_\beta = \left(\frac{\pi m^* q^2 \omega_o^2}{\hbar \kappa_0 \varepsilon_0 \beta^3 p \Omega}\right)\left(\frac{\kappa_0}{\kappa_\infty} - 1\right) \text{ (POP)} \tag{4.43},$$

$$C_\beta = \left(\frac{q e_{PZ}}{\kappa_S \varepsilon_0}\right)^2 \frac{\pi m^*}{\hbar^2 \rho \upsilon_S \beta^2 p \Omega} \text{ (PZ)} \tag{4.44}.$$

The general expression for the relaxation rate and the momentum relaxation rate for phonons can be derived using Eq. (4.40). For the relaxation rate, Eq. (4.40) is inserted into Eq. (4.17). Since the mapping between the momentum and the phonon wave vector is unique, as indicated in Eq. (4.35), the summation of Eq. (4.17) is taken over β instead of p. Transforming the summation into an integral gives the relaxation rate

$$\frac{1}{\tau} = \frac{\Omega}{8\pi^3} \int_0^{2\pi} d\phi \int_0^{\infty} C_\beta \left(N_\beta + \frac{1}{2} \mp \frac{1}{2}\right) \beta^2 d\beta$$

$$\times \int_{-1}^{1} \delta\left(\pm cos\,\theta + \frac{\hbar\beta}{2p} \mp \frac{\omega_\beta}{\upsilon\beta}\right) d(cos\,\theta) \tag{4.45}.$$

Mathematically, the delta function in this integral is zero unless $-1 < \frac{\hbar\beta}{2p} \mp \frac{\omega_\beta}{\upsilon\beta} < 1$. Therefore, this puts a restriction on the minimum and maximum values the phonon wave

vector may take. In physical terms, this restricts the phonon wave vector to the minimum and maximum values for which both momentum and energy are conserved. The relaxation time expression can therefore be simplified to

$$\frac{1}{\tau} = \frac{\Omega}{4\pi^2}\int_{\beta_{min}}^{\beta_{max}} C_\beta \left(N_\beta + \frac{1}{2} \mp \frac{1}{2}\right)\beta^2 d\beta \tag{4.46}$$

The momentum relaxation rate is evaluated in a similar manner by converting the summation in Eq. (4.18) into an integral. This is done by converting the last quantity in parenthesis to

$$\left(1 - \frac{p'}{p}\cos\alpha\right) = 1 - \frac{\boldsymbol{p}\cdot(\boldsymbol{p} \pm \hbar\boldsymbol{\beta})}{p^2} = \mp\frac{\hbar\beta\cos\theta}{p} \tag{4.47}$$

The momentum relaxation rate can then be written as

$$\frac{1}{\tau_m} = \frac{\Omega}{8\pi^3}\int_0^{2\pi} d\phi \int_0^{\infty} C_\beta \left(N_\beta + \frac{1}{2} \mp \frac{1}{2}\right)\beta^2 d\beta$$

$$\times \int_{-1}^{1} \delta\left(\pm cos\,\theta + \frac{\hbar\beta}{2p} \mp \frac{\omega_\beta}{\upsilon\beta}\right)\left(\mp\frac{\hbar\beta\cos\theta}{p}\right) d(cos\,\theta) \tag{4.48}$$

which, using the properties of the delta function, can immediately be simplified to

$$\frac{1}{\tau_m} = \frac{\Omega}{4\pi^2}\int_{\beta_{min}}^{\beta_{max}} C_\beta \left(N_\beta + \frac{1}{2} \mp \frac{1}{2}\right)\frac{\hbar\beta^3}{p}\left(\frac{\hbar\beta}{2p} \mp \frac{\omega_\beta}{\upsilon\beta}\right) d\beta \tag{4.49}$$

4.3.4. Non-Polar Acoustic Deformation Potential Scattering

The scattering of electrons in semiconductors by non-polar acoustic mode phonons was first proposed by Bardeen and Shockley [35]. Intra-valley acoustic phonons scattering is due to long-wavelength displacements, which is to say they have wave vectors very close to the origin of the Brillouin zone. The energy change of carriers involved in collisions with these phonons is very small, and therefore the scattering event

is usually taken to be elastic. In addition, scattering by non-polar acoustic modes are isotropic, so the relaxation rate and momentum relaxation rate are equal.

In order to evaluate the relaxation time for acoustic deformation potential scattering, Eq. (4.46) is used in conjunction with Eq. (4.41). For temperatures above a few degree Kelvin, the number of phonons is large so that $N_\beta \approx N_\beta + 1$ and the law of equipartition can be invoked, giving $N_\beta \approx k_B T_L/\hbar\omega_\beta$. The resulting relaxation rate is

$$\frac{1}{\tau_{ADP}} = \frac{m^* D_A^2 k_B T_L}{2\pi\hbar^2 v_S^2 \rho}\int_{\beta_{min}}^{\beta_{max}} \beta d\beta = \frac{m^* D_A^2 k_B T_L}{4\pi\hbar^2 v_S^2 \rho}\left(\beta_{max}^2 - \beta_{min}^2\right) \qquad (4.50).$$

The maximum and minimum phonon wave vectors can be deduced by using energy and momentum conservation laws with the assumption of spherical, parabolic energy bands, with the result being $\hbar\beta_{max} = 2m^* v$ and $\hbar\beta_{min} = 0$. The relaxation rate using these limiting phonon wave vectors is

$$\frac{1}{\tau_{ADP}} = \frac{1}{\tau_{m,ADP}} = \frac{m^* D_A^2 k_B T_L}{\hbar v_S^2 \rho} g(E) \qquad (4.51)$$

where $g(E)$ is the three dimensional density of states given by

$$g(E) = \frac{m^*\sqrt{2m^* E}}{\pi^2\hbar^3} \qquad (4.52).$$

Thus, acoustic deformation potential scattering is proportional to the number of final states available to carriers.

4.3.5. Piezoelectric Scattering

For crystals lacking inversion symmetry, elastic strain also causes an electrostatic perturbation that results in additional scattering. Scattering by acoustic phonons of this type is known as piezoelectric scattering, and is important at low temperatures and for high purity crystals. The microscopic origins of piezoelectricity were investigated

experimentally by Arlt and Quadflieg [36], who identified the piezoelectric effect as arising from ionic polarization, strain-dependent iconicity and electric polarization.

To obtain the momentum relaxation rate for piezoelectric scattering, Eq. (4.44) is inserted into Eq. (4.49). Invoking the law of equipartition and using the approximation $\omega_\beta \approx v_S\beta$ for acoustic wave vectors close to the origin results in

$$\frac{1}{\tau_{m,PZ}} = \left(\frac{qe_{PZ}}{\kappa_S\varepsilon_0}\right)^2 \frac{k_B T_L m^*}{4\pi\hbar\rho v_S^2 p^2} \int_{\beta_{min}}^{\beta_{max}} \left(\frac{\hbar\beta}{2p} \mp \frac{v_S}{v}\right) d\beta \qquad (4.53).$$

The piezoelectric effect is highly structure dependent, and this is reflected through the directional nature of the elastic constants implicit in the velocity of sound. This can be averaged out by defining a dimensionless value P, known as the electromechanical coupling coefficient, that groups together the piezoelectric constant, the density, and the sound velocity. In addition, since the velocity of sound is typically orders of magnitude smaller than the thermal carrier velocity, the second term in the integrand of Eq. (4.53) can be ignored. Carrying out the integration with the maximum and minimum wave vectors for acoustic phonons and multiplying by two to take account of both absorption and emission results in a momentum relaxation rate

$$\frac{1}{\tau_{m,PZ}} = \frac{q^2 k_B T_L P^2}{2\pi\kappa_S\varepsilon_0\hbar^2\sqrt{2E/m^*}} \qquad (4.54).$$

4.3.6. Polar Optical Phonon Scattering

Like piezoelectric scattering, polar optical phonon scattering arises from the long-range macroscopic electric fields created by the vibrations of oppositely charged atoms in a unit cell. For compound materials, polar optical phonon scattering is the dominant scattering mechanism. It is not isotropic and, unlike all the other scattering mechanisms discussed so far, is inelastic. The energy of optical phonons is comparable to $k_B T$ at room temperature, and this must be taken into account in any quantitative theory.

As will be seen in the next chapter, since polar optical phonon scattering is not isotropic or elastic, what is desired for mobility calculations is the relaxation rate rather than the momentum relaxation rate. This is accomplished by using Eq. (4.43) in Eq. (4.46). The maximum and minimum phonon wave vectors in this case can be found by setting the argument of Eq. (4.40) to zero and solving for β. The quadratic equation resulting from setting the argument of the delta function to zero is

$$\beta^2 \pm \frac{(2\mathrm{pcos}\,\theta)}{\hbar}\beta \mp \frac{2p\omega_o}{\hbar v} = 0 \tag{4.55}$$

where $\hbar\omega_o$ is the energy of the optical branch of the phonon dispersion relation. For long-wavelength (small wave vector) phonons, this value is approximately constant. The maximum wave vector occurs when $\cos\theta = -1$, while the minimum occurs when $\cos\theta = 1$, resulting in

$$\beta_{max} = \frac{p}{\hbar}\left(1 \pm \sqrt{1 \pm \frac{\hbar\omega_o}{E}}\right) \tag{4.56}$$

and

$$\beta_{max} = \frac{p}{\hbar}\left(\mp 1 \pm \sqrt{1 \pm \frac{\hbar\omega_o}{E}}\right) \tag{4.57}.$$

Using these limits in the integral of Eq. (4.46) gives the polar optical phonon relaxation time,

$$\frac{1}{\tau_{m,POP}} = \frac{q^2\omega_o\left(\frac{\kappa_0}{\kappa_\infty} - 1\right)}{4\pi\kappa_0\varepsilon_0\hbar\sqrt{2E/m^*}}$$

$$\left[N_o \ln\left(\frac{\sqrt{E+\hbar\omega_0}+\sqrt{E}}{\sqrt{E+\hbar\omega_0}-\sqrt{E}}\right) + (N_o+1)\ln\left(\frac{\sqrt{E}+\sqrt{E-\hbar\omega_0}}{\sqrt{E}-\sqrt{E-\hbar\omega_0}}\right)\right] \tag{4.58}$$

where N_o is the optical phonon occupation number determined by Bose-Einstein statistics

$$N_o = \frac{1}{e^{\hbar\omega_o/k_BT} + 1} \tag{4.59}$$

The first term in brackets in Eq. (4.58) represents absorption of an optical phonon, while the second represents emission of an optical phonon. It is understood that the second term in the brackets only applies when the carrier energy is greater than or equal to the optical phonon energy.

4.3.7. Inter-valley Phonon Scattering

In addition to the phonon scattering processes discussed in the previous sections, both acoustic and optical phonons can scatter carriers from one valley of the band structure into another. The final valley the carriers scatter into may either be energetically equivalent to the initial valley, or it may be a valley that is not energetically equivalent. The scattering into energetically equivalent valleys involves large changes in momentum, and therefore result from short-wavelength phonons with wave vectors close to the Brillouin zone boundary. In this region, acoustic and optical phonons have energies that approach similar values. In addition, carriers can scatter to a final valley that is not energetically equivalent. This can either take the form of scattering between extrema at different points in the Brillouin zone, or between extrema at the same point but at different energies. In all of these cases, the mechanism is approximated to be isotropic since non-polar inter-valley scattering is a randomizing process. While this does not hold true for polar processes, piezoelectric and polar optical phonon inter-valley scattering is typically unimportant except for very low temperatures.

The relaxation rate for inter-valley phonons can be found in a phenomenological manner by treating the perturbing potential as

$$U_S = D_{if} u_\beta \tag{4.60}$$

where D_{if} is the deformation potential describing inter-valley scattering. Thus, the factor $\left|K_{\beta}\right|^2$ is just D_{if}^2. Using this in the relaxation rate integral of Eq. (4.46) gives the result

$$\frac{1}{\tau_{if}} = \frac{1}{\tau_{m,if}} = \frac{\pi D_{if}^2 Z_f}{\rho \omega_{if}}$$

$$\times \left[N_i \, g\left(E + \hbar\omega_{if} - \Delta E_{if}\right) + (N_i + 1) \, g\left(E - \hbar\omega_{if} - \Delta E_{if}\right)\right] \qquad (4.61)$$

where Z_f is the number of final valleys available at the extrema under consideration, $\hbar\omega_{if}$ is the inter-valley phonon energy, N_i is the inter-valley phonon occupation number determined by Eq. (4.59), and ΔE_{if} is the difference in energy between the initial and final valleys. Since only phonons close to the zone boundary, where the acoustic and optical phonon dispersion curves flatten out and approach the same value, are involved in inter-valley scattering, $\hbar\omega_{if}$ is approximated as a constant value. Again, the first term in brackets indicates absorption while the second term indicates emission, with emission only possible if the carrier energy is greater than the sum of the inter-valley phonon energy and the energy difference between the initial and final valleys. For inter-valley scattering to energetically equivalent valleys, ΔE_{if} is zero.

CHAPTER 5. TRANSPORT IN 6H SIC

5.1. Introduction

During the last few decades, the various polytypes of silicon carbide (SiC) have been intensively studied in the hope that it will become a suitable material for high-power and high-temperature electronic applications. The 4H polytype of SiC has garnered the most attention because its band gap is the largest of the various polytypes, while the more developed 6H polytype of SiC is already an important substrate material for optoelectronic applications. However, for any practical realization of electronic devices on SiC to occur, certain transport properties need to be known. One such quantity is the electron mobility, and to this end experimental studies have been carried out to determine its value [37-42]. Along with these experimental results are theoretical calculations that attempt to model them and to explain the mechanisms that determine the mobility [38-40,43-46]. The scattering theory discussed in the previous chapter provides a natural avenue to investigate these mechanisms, since they provide a microscopic description of the processes that factor into the determination of the mobility. Indeed, many theoretical studies have relied on such a treatment to explain the electron mobility for both 4H and 6H SiC [38,39,43-46].

In terms of 6H SiC, while the aforementioned computational studies had adequate success in explaining the experimental results, all of these calculations have either: (i) focused on calculating the electron drift mobility, while the experimental work has usually measured the electron Hall mobility, or (ii) been inexact solutions based on the relaxation time approximation. Comparisons between the Hall mobility and drift mobility have been justified by either assuming a Hall scattering factor of unity, or through a calculation of the Hall scattering factor which also relied on the relaxation time approximation. Experiments have shown that the former assumption can be off by as

much as 19% depending on temperature and doping concentration [47]. Meanwhile, Hall scattering factors calculated with the relaxation time approximation differ significantly from experimental data [43].

In this chapter a more accurate calculation of the electron Hall mobility and Hall scattering factor for 6H-SiC is presented by calculating the electron Hall mobility exactly using the contraction mapping principle [48]. At the same time, the low field electron drift mobility is solved exactly using Rode's iterative method [49], and the Hall scattering factor is then arrived at by taking the ratio of the two values multiplied by a mass factor. Similar calculations have been applied to 4H SiC, giving more accurate computational results compared to past studies [38]. However, those techniques have not yet been applied to 6H SiC until now [50]. In addition, a single set of values for the acoustic deformation potential, the intervalley deformation potential and the intervalley phonon energy, which are adjusted to simultaneously match the experimental Hall scattering factor and Hall mobility data, are given. The calculated electron Hall mobilities and Hall scattering factors are compared with the experimental data of Karmann *et al.* [41] and Rutsch *et al*. [47], respectively. Finally, how the change of ionization energy with impurity concentration affects the mobility calculation will be briefly explored. First, however, a concise overview of the techniques used to solve the Boltzmann transport equation is given.

5.2. Solving the Boltzmann Transport Equation for Mobility and the Hall Scattering Factor

The general approach in statistical mechanics for finding thermodynamic quantities of interest for an ensemble of particles is to first find the partition function, from which the distribution function can be deduced [51]. The distribution function measures the probability of finding carriers at a given location, possessing a given momentum, at a

given time, and from which quantities such as conductivity and mobility can be computed [27]. At equilibrium, the distribution function for fermionic particles is just the Fermi-Dirac function. Interactions with electric and magnetic fields as well as scattering events, cause deviations from the equilibrium distribution function. Deviations from the equilibrium distribution function in response to these stimuli can be deduced through the use of Louisville's theorem or, more commonly in the field of semiconductors, a more specialized version of Louisville's theorem known as the Boltzmann equation [27,28].

The Boltzmann equation can be derived by carefully tracking carrier in-flows and out-flows in a given volume of six-dimensional phase space, which is made up of three dimension in position and three dimensions in momentum. Doing so gives the time evolution of the distribution function as

$$\frac{\partial f}{\partial t} = -\left(\boldsymbol{v}\cdot\nabla_{\boldsymbol{r}} f + \frac{q\boldsymbol{F}}{\hbar}\cdot\nabla_{\boldsymbol{k}} f\right) + \left.\frac{\partial f}{\partial t}\right|_{coll} + s(\boldsymbol{r},\boldsymbol{k},t) \qquad (5.1)$$

where **F** is the electric field. The first term in parenthesis on the right hand side of Eq. (5.1) represents the net in- or out-flow in position and momentum space, respectively. The second term is known as the collision integral and is the change in distribution due to scattering events. This can be due to carriers with a momentum $\boldsymbol{k}'$ in-scattering to the wave vector $\boldsymbol{k}$ or carriers in wave vector $\boldsymbol{k}$ out-scattering to a wave vector $\boldsymbol{k}'$. In either case, this will depend on the probability that the original state is filled and the probability that the final state is empty, resulting in

$$\left.\frac{\partial f}{\partial t}\right|_{coll} = \sum_{\boldsymbol{k}'} S_{\boldsymbol{k}',\boldsymbol{k}} f_{\boldsymbol{k}'}(1-f_{\boldsymbol{k}}) - \sum_{\boldsymbol{k}'} S_{\boldsymbol{k},\boldsymbol{k}'} f_{\boldsymbol{k}}(1-f_{\boldsymbol{k}'}) \qquad (5.2).$$

For non-degenerate semiconductors, the distribution function is much less than unity so that Eq. (5.2) can be approximated as

$$\left.\frac{\partial f}{\partial t}\right|_{coll} = \sum_{\boldsymbol{k'}} S_{\boldsymbol{k'},\boldsymbol{k}} f_{\boldsymbol{k'}} - \sum_{\boldsymbol{k'}} S_{\boldsymbol{k},\boldsymbol{k'}} f_{\boldsymbol{k}} \qquad (5.3).$$

Finally, the last term on the right hand side of Eq. (5.1) is the net generation recombination rate in the volume of phase space.

For semiconductors, what is typically of interest is the low field mobility. Under these steady-state, spatially homogeneous conditions with Fermi-Dirac statistics, the Boltzmann equation becomes

$$-\frac{q\boldsymbol{F}}{\hbar}\cdot\nabla_{\boldsymbol{k}} f_{\boldsymbol{k}} = \int \left[S_{\boldsymbol{k'},\boldsymbol{k}}(1-f_{\boldsymbol{k}})f_{\boldsymbol{k'}} - S_{\boldsymbol{k},\boldsymbol{k'}} f_{\boldsymbol{k}}(1-f_{\boldsymbol{k'}})\right] d\boldsymbol{k'} \qquad (5.4)$$

where the summations of Eq. (5.3) have been converted to integrals. The second term on the right hand side of Eq. (5.4), which describes out-scattering processes, can be integrated in a straight forward manner. However, the first term on the right hand side, which describes in-scattering processes, depends on the unknown distribution function and cannot be so easily computed.

In order to proceed, the distribution function is written as

$$f_{\boldsymbol{k}} = f_{0,\boldsymbol{k}} + x g_{\boldsymbol{k}} \qquad (5.5)$$

where $f_{0,\boldsymbol{k}}$ is the equilibrium distribution function, $g_{\boldsymbol{k}}$ is the perturbed distribution function, and x is the cosine of the angle between the electric field $\boldsymbol{F}$ and the wave vector $\boldsymbol{k}$. This result can be shown to be true for electrons in spherical bands under low fields. Inserting Eq. (5.5) into Eq. (5.4) and only keeping terms involving x gives

$$-\frac{qF}{\hbar}\frac{\partial f_0}{\partial k} = -\int g_{\boldsymbol{k}}\left[S_{\boldsymbol{k},\boldsymbol{k'}}\left(1-f_{0,\boldsymbol{k'}}\right) - S_{\boldsymbol{k'},\boldsymbol{k}} f_{0,\boldsymbol{k'}}\right] d\boldsymbol{k'}$$

$$+\int x g_{\boldsymbol{k'}}\left[S_{\boldsymbol{k'},\boldsymbol{k}}\left(1-f_{0,\boldsymbol{k}}\right) - S_{\boldsymbol{k},\boldsymbol{k'}} f_{0,\boldsymbol{k}}\right] d\boldsymbol{k'} \qquad (5.6)$$

At this point, it is advantageous to divide the scattering mechanisms into those due to elastic processes and those due to inelastic processes. By doing so, Eq. (5.6) becomes

$$-\frac{qF}{\hbar}\frac{\partial f_0}{\partial k} = -\int g_{\boldsymbol{k}}\left[S^{inel}_{\boldsymbol{k},\boldsymbol{k}'}\left(1-f_{0,\boldsymbol{k}'}\right) - S^{inel}_{\boldsymbol{k}',\boldsymbol{k}} f_{0,\boldsymbol{k}'}\right]d\boldsymbol{k}' - g_{\boldsymbol{k}}\upsilon_{el}$$

$$+\int x g_{\boldsymbol{k}'}\left[S^{inel}_{\boldsymbol{k}',\boldsymbol{k}}\left(1-f_{0,\boldsymbol{k}}\right) - S^{inel}_{\boldsymbol{k},\boldsymbol{k}'} f_{0,\boldsymbol{k}}\right]d\boldsymbol{k}' \qquad (5.7)$$

where $S^{inel}_{\boldsymbol{k}',\boldsymbol{k}}$ and $S^{inel}_{\boldsymbol{k},\boldsymbol{k}'}$ are the transition rates due to inelastic processes. The elastic processes, υ_{el}, are grouped together and, because $\boldsymbol{k}$ and $\boldsymbol{k}'$ are equal in this case, are reduced to

$$\upsilon_{el} = \int S^{el}_{\boldsymbol{k},\boldsymbol{k}'}(1-\cos\alpha)d\boldsymbol{k}' \qquad (5.8),$$

where $S^{el}_{\boldsymbol{k},\boldsymbol{k}'}$ is the transition rate due to elastic processes. This is just the definition of the momentum relaxation rate (see Eq. (4.18)), so that υ_{el} is just the sum of the momentum relaxation rates of all the relevant out-scattering elastic processes. Finally, by rearranging Eq. (5.7) an iterative form can be found for the unknown distribution function,

$$g_{\boldsymbol{k},i+1} = \frac{S_i\left(g_{\boldsymbol{k},i}\right) + \frac{qF}{\hbar}\frac{df_0}{dk}}{S_o} \qquad (5.9)$$

where S_o is the sum of the out-scattering processes and is given by

$$S_o = \upsilon_{el} + {}^1\!/_{\tau_{in}} \qquad (5.10).$$

In the previous two expressions, the inelastic scattering processes have been grouped into two different terms. The first represents the out-scattering inelastic processes and is given by

$${}^1\!/_{\tau_{in}} = \int\left[S^{inel}_{\boldsymbol{k},\boldsymbol{k}'}\left(1-f_{0,\boldsymbol{k}'}\right) - S^{inel}_{\boldsymbol{k}',\boldsymbol{k}} f_{0,\boldsymbol{k}'}\right]d\boldsymbol{k}' \qquad (5.11).$$

As previously mentioned, for non-degenerate semiconductors the distribution function is much less than unity, so that Eq. (5.10) can be approximated as

$$1/\tau_{in} = \int S^{inel}_{\boldsymbol{k},\boldsymbol{k}'} d\boldsymbol{k}' \tag{5.12},$$

which shows that the inelastic out-scattering terms are just the sum of the relaxation rates of the individual processes (see Eq. (4.17)). The other term describes in-scattering due to inelastic processes, and is given by the integral

$$S_i(g_{\boldsymbol{k}}) = \int x g_{\boldsymbol{k}'} \left[S^{inel}_{\boldsymbol{k}',\boldsymbol{k}} (1 - f_{0,\boldsymbol{k}}) - S^{inel}_{\boldsymbol{k},\boldsymbol{k}'} f_{0,\boldsymbol{k}} \right] d\boldsymbol{k}' \tag{5.13}.$$

For each relevant inelastic process, the integral of Eq. (5.13) must be solved. The iterative form of Eq. (5.10) can be shown to be a contraction mapping that leads to quickly converging solutions.

After solving the perturbed distribution function to arbitrary accuracy using Eq. (5.10), the drift mobility is calculated by

$$\mu = -\frac{\hbar}{3m^*} \frac{\int \boldsymbol{k}^3 (g_{\boldsymbol{k}}/F) d\boldsymbol{k}}{\int \boldsymbol{k}^2 f_0 d\boldsymbol{k}} \tag{5.14}$$

where μ is the electron drift mobility, $\hbar$ is the reduced Planck constant, and m^* is the effective mass of the electron. This iterative technique to solve for the mobility in the presence of a low electric field was first discussed by Rode in 1975 [49].

A similar contraction mapping technique, also introduced by Rode [48], solves the Boltzmann transport equation in the presence of an arbitrary magnetic field. In this case, the distribution function is given by

$$f_{\boldsymbol{k}} = f_0 + x g_{\boldsymbol{k}} + y h_{\boldsymbol{k}} \tag{5.15}$$

where $h_{\mathbf{k}}$ is the perturbation distribution function due to the magnetic field, and y is the direction cosine from $\mathbf{B} \times \mathbf{F}$ to $\mathbf{k}$. Insertion of Eq. (5.15) into Eq. (5.1) yields a coupled pair of equations that can be solved iteratively,

$$g_{\boldsymbol{k},i+1} = \frac{S_i(g_{\boldsymbol{k},i}) + \frac{qF}{\hbar}\frac{df_0}{dk} + \beta S_i(h_{\boldsymbol{k}})}{S_0(1+\beta^2)} \tag{5.16}.$$

and

$$h_{\boldsymbol{k},i+1} = \frac{S_i(h_{\boldsymbol{k},i}) - \beta\frac{qF}{\hbar}\frac{df_0}{dk} + \beta S_i(g_{\boldsymbol{k}})}{S_0(1+\beta^2)} \tag{5.17}$$

where $\beta = qvB/\hbar k S_o$, v is the electron group velocity, and B is the magnetic field. In a similar manner to Eq. (5.14), these two perturbed distribution functions yield the electron Hall mobility μ_H as

$$\mu_H = \frac{\int \boldsymbol{k}^3 (h_{\boldsymbol{k}}/B) d\boldsymbol{k}}{\int \boldsymbol{k}^2 g_{\boldsymbol{k}} d\boldsymbol{k}} \tag{5.18}.$$

With the drift mobility and Hall mobility determined, the Hall scattering factor r_H is given by

$$r_H = \frac{\mu_H}{\mu} \tag{5.19}$$

This solution is a more accurate calculation of the Hall scattering factor compared to the more commonly used expression

$$r_H = \frac{\langle\langle \tau^2 \rangle\rangle}{\langle\langle \tau \rangle\rangle^2} \tag{5.20}$$

where $\langle\langle \tau^2 \rangle\rangle$ and $\langle\langle \tau \rangle\rangle^2$ are the specially averaged scattering times. The latter expression for the Hall scattering factor is derived from the relaxation time approximation, which assumes that scattering times are independent of the distribution function. More importantly, the relaxation time approximation is only valid when the scattering

processes are either elastic or isotropic, which is not true for 6H SiC where polar optical phonon scattering dominates the low-field mobility (this scattering mechanism is neither elastic nor isotropic).

5.3. Scattering Mechanisms in 6H SiC

In order to calculate S_o and S_i and properly determine the Hall and drift mobilities, the relevant scattering mechanisms must be taken into account. For 6H SiC in this study, six scattering mechanisms are considered: (i) acoustic deformation potential scattering, (ii) ionized impurity scattering, (iii) neutral impurity scattering, (iv) piezoelectric scattering, (v) inter-valley phonon deformation potential scattering, and (vi) polar optical phonon scattering.

The values of the acoustic deformation potential, inter-valley phonon deformation potential, and inter-valley phonon energy were taken as adjustable parameters to simultaneously fit the Hall scattering factor and Hall mobility data (as will be discussed later). An acoustic deformation potential D_A value of 5.5 eV, an inter-valley phonon deformation potential D_{if} value of 1.25×10^{11} eV/m and inter-valley phonon energy $\hbar\omega_{if}$ of 65 meV was found to best fit the experimental mobility data. In addition, parabolic conduction bands are assumed, with the values of the effective masses for 6H SiC being $m^*_{\mathrm{M\Gamma}}(m_1^*) = 0.75m_0$, $m^*_{MK}(m_2^*) = 0.24m_0$, and $m^*_{ML}(m_3^*) = 1.83m_0$, and the density of states effective mass being $m^* = (m_1^* m_2^* m_3^*)^{1/3}$ [26]. Material properties of 6H SiC that were used included a relative dielectric constant κ_S of 9.7, a speed of sound v_S of 13,730 m/s^2 and mass density ρ of 3211 kg/m^3 [52]. For the mobility with the electric field perpendicular to the *c* axis of the crystal, the coupling coefficient P for hexagonal structures is

$$P^2 = \frac{4\left(21e_{15}^2 + 6e_{15}e_x + e_x^2\right)}{105\kappa_s\varepsilon_0 c_t} + \frac{(21e_{33}^2 - 24e_{33}e_x + 5e_x^2)}{105\kappa_s\varepsilon_0 c_l} \qquad (5.21)$$

where $e_x = e_{33} - e_{31} - 2e_{15}$, and e_{15}, e_{31}, and e_{33} are the piezoelectric constants. The averaged transverse and longitudinal elastic constants for wurzite structures, c_t and c_l, are given by

$$c_l = \frac{8c_{11} + 4c_{13} + 3c_{33} + 8c_{44}}{15} \tag{5.22}$$

$$c_t = \frac{2c_{11} - 4c_{13} + 2c_{33} + 7c_{44}}{15} \tag{5.23}$$

where c_{11}, c_{13}, c_{33} and c_{44} are the elastic constants. In this study, the piezoelectric constants calculated by Mirgorodsky *et al*. are used [53], while the elastic constants measured by Kamitani *et al.* are used [54].

For the two components that compose the out-scattering term S_o, all the relevant transition rates were derived in the previous chapter. The elastic component, υ_{el}, is the sum of the momentum relaxation rates of scattering processes (i)-(v) above. The inelastic component, $1/\tau_{in}$, is made up of the relaxation rate of polar optical scattering given by Eq. (4.58) and inter-valley phonon scattering given by Eq. (4.61). On the other hand, for the in-scattering term S_i the integral of Eq. (5.13) must be evaluated for inelastic processes. For mechanisms under consideration, this only includes (v) and (vi) above. As it turns out, the integral of Eq. (5.13) for inter-valley phonon scattering vanishes [49]. Therefore, Eq. (5.13) only needs to be evaluated for polar optical phonon scattering. Doing so gives [49]

$$S_i = \{N_o g(E_k - \hbar\omega_o)\lambda^- + (N_o + 1)g(E_k + \hbar\omega_o)\lambda^+\} \tag{5.24}$$

where

$$\lambda^{-} = \frac{q^2 \omega_o m^{*1/2}}{2^{5/2} \pi \varepsilon_0 \hbar E_k^{1/2}} \left(\frac{1}{\kappa_\infty} - \frac{1}{\kappa_0} \right)$$

$$\times \left(\frac{2E_k - \hbar\omega_o}{[E_k(E_k - \hbar\omega_o)]^{1/2}} ln \left| \frac{\sqrt{E_k + \hbar\omega_0} + \sqrt{E_k}}{\sqrt{E_k + \hbar\omega_0} - \sqrt{E_k}} \right| - 1 \right) \qquad (5.25)$$

and

$$\lambda^{+} = \frac{q^2 \omega_o m^{*1/2}}{2^{5/2} \pi \varepsilon_0 \hbar E_k^{1/2}} \left(\frac{1}{\kappa_\infty} - \frac{1}{\kappa_0} \right)$$

$$\times \left(\frac{2E_k + \hbar\omega_o}{[E_k(E_k + \hbar\omega_o)]^{1/2}} ln \left| \frac{\sqrt{E_k - \hbar\omega_0} + \sqrt{E_k}}{\sqrt{E_k - \hbar\omega_0} - \sqrt{E_k}} \right| - 1 \right) \qquad (5.26).$$

To see the relative importance of each of the scattering mechanisms in *n*-type 6H-SiC, the scattering rates for doping concentrations of $N_D = 10^{16} cm^{-3}$ and $N_D = 10^{19} cm^{-3}$ are shown in Fig. 5.1 and Fig. 5.2, respectively as a function of energy and temperature. Previous studies have indicated that the ratio of impurities at cubic sites to impurities at hexagonal sites is about 2:1 [41,42,47]. Therefore, for both of these plots, it is assumed that there are twice as many impurities at cubic sites than there are at hexagonal sites, and that there is no compensation. The free electron concentration is found by solving the charge neutrality equation

$$n + N_A = \frac{N_{DH}}{1 + g_H exp[(E_F - E_C + E_{DH})/(k_B T)]}$$

$$+ \frac{N_{DK}}{1 + g_K exp[(E_F - E_C + E_{DK})/(k_B T)]} \qquad (5.27)$$

where n is the electron concentration, N_A the acceptor compensation level, E_C is the conduction band minimum, E_F is the energy of the Fermi level, N_{DH} and N_{DK} are the concentrations of impurities at hexagonal and cubic sites, respectively, g_H and g_K are the donor degeneracy levels of the hexagonal and cubic levels, respectively, and E_{DH} and

E_{DK} are the ionization energies of the impurities at hexagonal and cubic sites, respectively. Both the donor degeneracy levels are assumed to be 2. For this example, the donor ionization energies were set at 94 meV and 118 meV for the hexagonal and cubic sites, respectively.

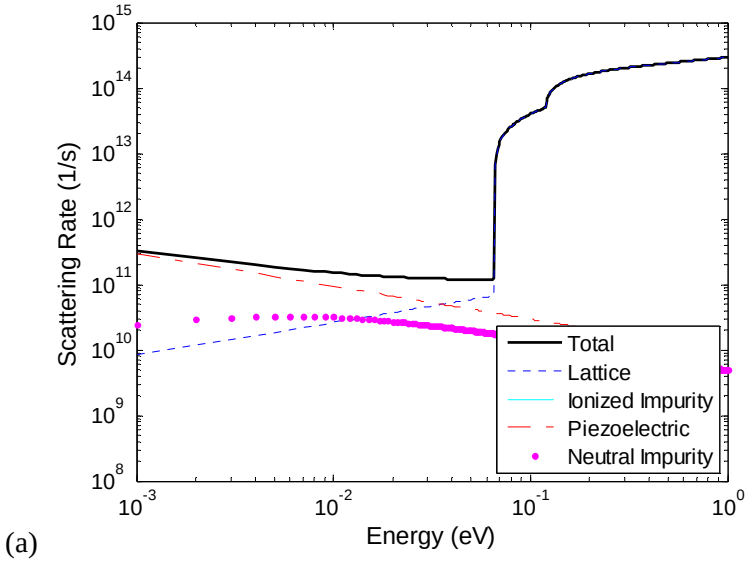

(a)

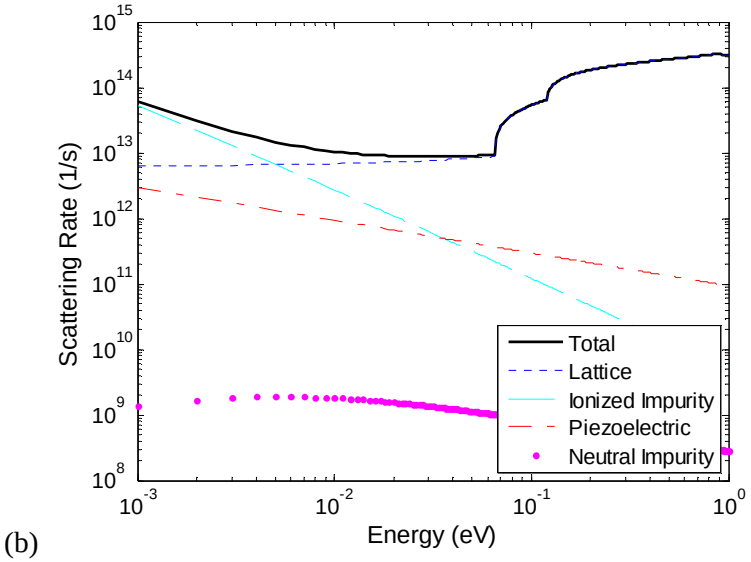

(b)

Fig. 5.1. Scattering rates versus energy for $N_D = 1 \times 10^{15}\text{cm}^{-3}$ at (a) 30 K and (b) 300 K.

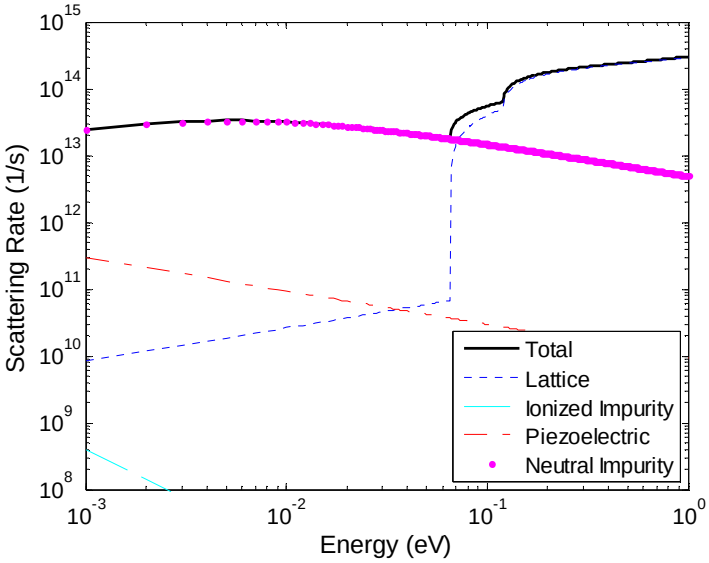

(a)

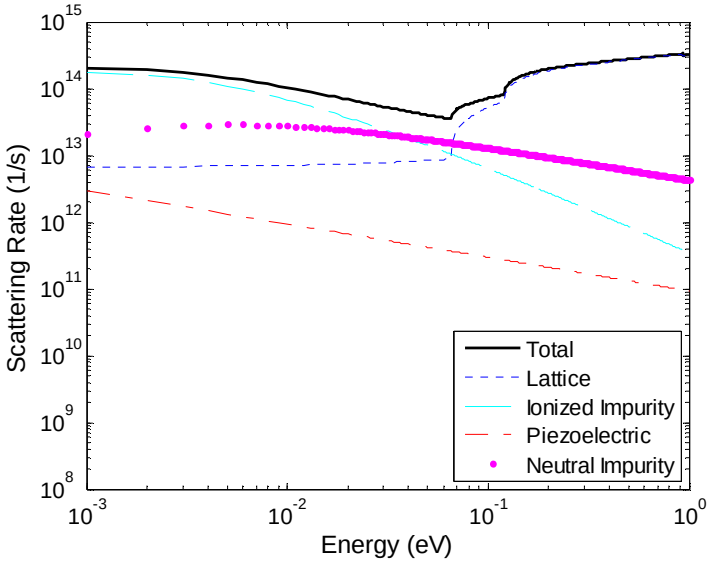

(b)

Fig. 5.2. Scattering rates versus energy for $N_D = 1 \times 10^{19}\text{cm}^{-3}$ at (a) 30 K and (b) 300 K.

The lattice scattering in these plots includes acoustic deformation potential, intervalley phonon, and polar optical phonon scattering. At lower temperatures for both doping concentrations, neutral impurity scattering is significant for lower energy carriers,

necessitating its inclusion as a scattering mechanism. In addition, at lower temperatures, piezoelectric scattering is the strongest scattering mechanism at lower doping concentrations while still being significant at higher doping concentrations for low energy carriers. All previous mobility and Hall scattering factor calculations have left this mechanism out, even while making calculations at lower temperatures [43-46]. At higher temperatures, ionized impurity scattering generally dominates. For lower doping concentrations, lattice scattering makes a significant contribution, while at higher doping concentrations, neutral impurity scattering is again important.

5.4. Electron Hall Mobility and Scattering Factor

Using Eq. (5.19) and the techniques discussed in section 5.2, and including the scattering mechanisms previously mentioned, the Hall mobility and the Hall scattering factor were calculated and were fit to the experimental data measured by Karmann *et al.* [41] and Rutsch *et al.* [47] These were calculated assuming a measurement configuration of $[\mathbf{B} \parallel \mathbf{c}, \mathbf{j} \perp \mathbf{c}]$ and with magnetic fields of $B = 0.4$ T T and $B = 0.741$ T T, as in the experiments. Because of the measurement configuration, a mass factor is included in the Hall scattering factor [43].

As previously mentioned, the values of the acoustic deformation potential, intervalley deformation potential, and intervalley phonon energy were adjusted to obtain a best fit for the Hall mobility and Hall scattering factor data simultaneously. In a manner similar to previous studies [43,55], the parameters were first adjusted to the Hall mobility data, and then subsequently used in the calculation of the Hall scattering factor data. For the most part, adjustment of the acoustic deformation potential had the effect of shifting the Hall mobility curve as higher or lower. Meanwhile, adjustment of the intervalley deformation potential and the intervalley phonon energy primarily affected the slope of the data at

temperatures above 100 K. Fig. 5.3 shows the comparison of the calculated and the experimental Hall mobility for three different samples, while Fig. 5.4 shows the comparison of the calculated and the experimental Hall scattering factor. The calculated results fit the experimental data very well. This is particularly true for the calculated Hall scattering factor, which matches experimental data more so than calculations with a relaxation time approximation by Iwata *et al.* [43] The deviation of the calculated Hall scattering factor in this study from experimental data never exceeds 8.8%.

However, the aforementioned fitting results in values of $D_A = 5.5$ eV, $D_{if} = 1.25 \times 10^{11}$ eV/m, and $\hbar\omega_{if} = 65$ meV, which diverge drastically from previously reported values of $D_A = 17.5$ eV, $D_{if} = 0.6 \times 10^{11}$ eV/m, and $\hbar\omega_{if} = 85.4$ meV [44,46]. This warrants some discussion. The first study to attempt to extract the deformation potentials and intervalley phonon energy (from which the latter set of parameters originated) by Mickevicius *et al.* [44] used a Monte Carlo method to calculate the electron drift mobility. This calculated mobility was then fit to experimental Hall data without accounting for the Hall scattering factor. A subsequent study by Dhar *et al.* [46] used the same set of parameters in a calculation of the drift mobility using Rode's iterative method. The Hall scattering factor in this case was calculated using Eq. (5.20), which is an inexact solution, and without using a mass factor to account for the anisotropy of the Hall measurement configuration. It is no surprise that the same set of parameters yields similar results for both the Monte Carlo and Rode's iterative method, as both are recognized as exact methods of obtaining the electron drift mobility. Neither method, however, solves for the Hall mobility. It can therefore be argued that the more accurate parameters are the ones obtained in this study.

Because of the large deviations of the Hall scattering factor from unity and its importance, it is clear that in order to deduce the electron drift mobility from

experimental Hall mobility data the Hall scattering factor must be accurately known. Fig. 5.5 shows predicted values of the Hall scattering factor against temperature at four different doping concentrations for $B = 0.5$ T. These calculated values assume a 2:1 ratio of impurities at cubic sites to impurities at hexagonal sites, and a compensation ratio of $N_A/N_D = 0.01$. These curves show that the doping concentration and the temperature both greatly impact the Hall scattering factor for the $[\mathbf{B} \parallel \mathbf{c}, \mathbf{j} \perp \mathbf{c}]$ Hall measurement configuration, so that extreme care must be taken when trying to extract the electron drift mobility from Hall measurements in 6H-SiC.

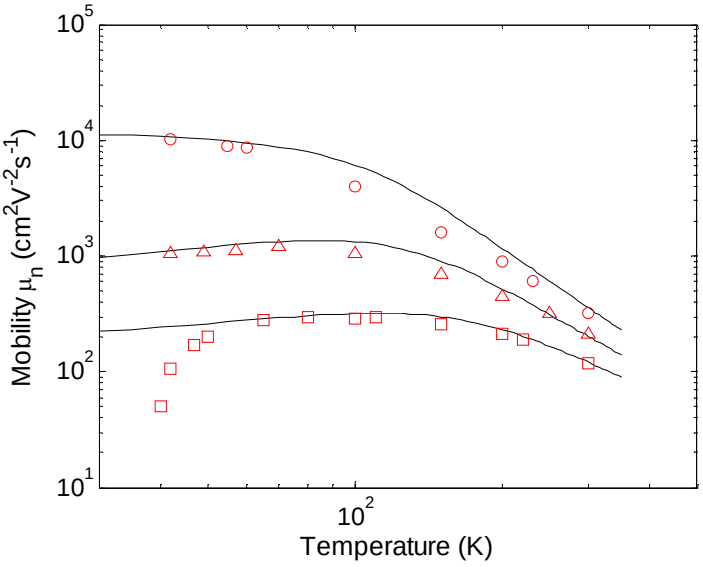

Fig. 5.3. Electron Hall mobility versus temperature at $B = 0.4$ T for (a) $N_{DH} = 3.5 \times 10^{15}\ cm^{-3}$, $N_{DK} = 7 \times 10^{15}\ cm^{-3}$, $N_A = 1 \times 10^{14}\ cm^{-3}$, $E_{DH} = 94\ meV$, and $E_{DK} = 118\ meV$, (b) $N_{DH} = 2 \times 10^{17}\ cm^{-3}$, $N_{DK} = 4 \times 10^{15}\ cm^{-3}$, $N_A = 1.7 \times 10^{15}\ cm^{-3}$, $E_{DH} = 90\ meV$, and $E_{DK} = 120\ meV$, (c) $N_{DH} = 4.4 \times 10^{16}\ cm^{-3}$, $N_{DK} = 3.4 \times 10^{18}\ cm^{-3}$, $N_A = 5.5 \times 10^{15}\ cm^{-3}$, $E_{DH} = 63\ meV$, and $E_{DK} = 120\ meV$ *n*-type 6H-SiC. Solid lines are calculated, while the symbols are experimental data taken from Karmann *et al.*

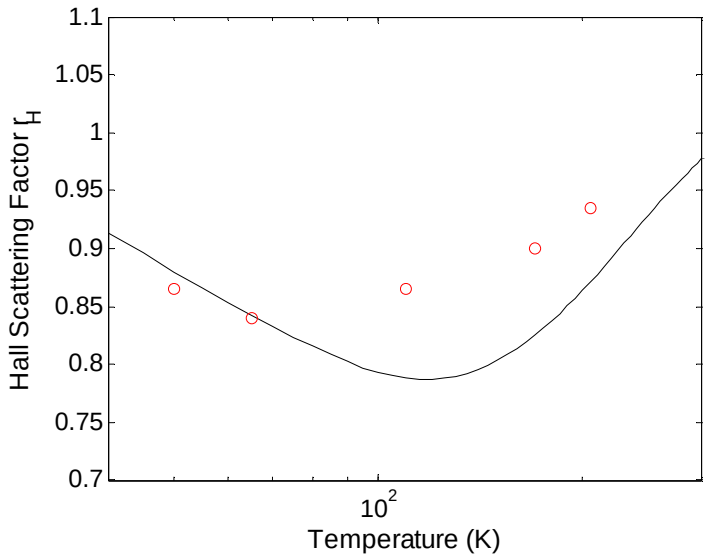

Fig. 5.4 Hall scattering factor versus temperature at $B = 0.741$ T for $N_{DH} = 3.3 \times 10^{15}\ cm^{-3}$, $N_{DK} = 5.7 \times 10^{15}\ cm^{-3}$, $E_{DH} = 112\ meV$, and $E_{DK} = 157\ meV$ for *n*-type 6H-SiC. Solid lines are calculated, while the symbols are experimental data taken from Rutsch *et al.*

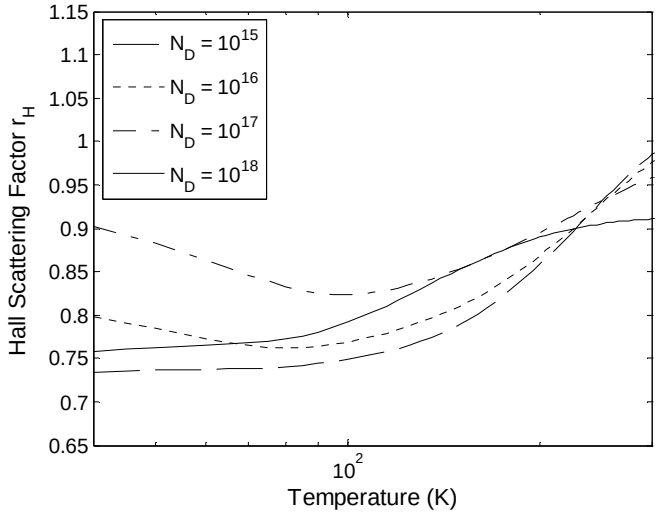

Fig. 5.5 Predicted values of the Hall scattering factor plotted against temperature with doping concentration as a parameter for *n*-type 6H-SiC.

5.5. Investigation of Ionization Energy Variation

Apparent from Fig. 5.3 is that the calculation does not give good agreement for higher doping concentrations at lower temperatures. This would be indicative that one of the scattering mechanisms considered is stronger at high doping concentration and low temperatures, or that an entirely different mechanism is involved under these circumstances. One possible explanation for this deviation is the lowering of the ionization energy due to a higher density of impurities. Such a lowering would result in an increase in ionized impurities, and consequently an increase in the corresponding scattering rate. Thus, at lower temperatures and higher doping concentration where neutral impurity scattering traditionally dominates, there would be a relative increase in the stronger ionized impurity scattering.

The phenomenon of decreasing ionization energy with increasing impurity concentrations has been observed since the earliest studies of the behavior of impurities in semiconductors. Pearson and Bardeen noted it in their study of impurities in Si [56], while Brooks further elucidated upon this effect in discussing impurities in Si and germanium (Ge) [57]. The effect has also been observed in GaAs [58] and aluminum (Al) acceptors in 6H SiC [59]. The decrease in the impurity ionization energy arises from a reduction in the average potential energy of carriers. As the impurity concentration increases, the excited states of the impurities overlap and shield the potential of the ions. Mathematically, the decrease in the ionization energy can be described by [56]

$$E_I = E_{I0} - \alpha N^{1/3} \tag{5.28}$$

where E_I is the impurity concentration dependent ionization energy, E_{I0} is the ionization energy for low doping, α is the factor by which the ionization energy reduced. Typically, α is experimentally determined. However, a rough order-of-magnitude estimate has been

given by Pearson and Bardeen [56]. Accounting for energy of attraction between the ion and mobile carriers, and the self-energy and correlation energies, the reduction factor is given by

$$\alpha = \frac{1.646q^2}{4\pi\varepsilon_S\varepsilon_0} \tag{5.29}.$$

The adjustment to the ionization energies given in Eq. (5.28) and (5.29) were applied to the calculation of mobility of electrons in 6H SiC in the preceding section. Fig. 5.6 shows the changes to the scattering rates for high doping concentration and low temperatures as well as the changes to the Hall mobility curves when the approximate decrease in ionization energy is accounted for. As expected, the mobility curves for lower doping concentrations are not visibly affected. For the highly doped curve, the mobility is most noticeably affected at temperatures above about 40 K. This is the result of the significant increase of ionized impurity scattering. Below 40 K, the mobility begins to rise again. At this temperature range, impurities remain largely unionized since the thermal energy is so low. Thus, ionized impurity scattering is less of a factor as shown by the scattering rates in Fig. 5.6.

The poor fit of the calculated mobility curve with doping-dependent ionization energies at low temperatures for high doping concentrations indicate that this is not the explanation for the decrease in the experimental Hall mobility data at lower temperatures. In addition, the discrepancy between the calculated and experimental Hall mobility for the more highly doped curve in comparison to the more lightly doped curves further indicate this. However, it should also be noted that Eq. (5.29) used in this calculation is a very rough, order of magnitude estimate. In addition, the previously mentioned study of Al impurities in 6H-SiC indicated that α in that case was compensation as well as doping dependant. Since α is usually experimentally measured, it may still be the case that the

decrease in ionization energy is the reason for the decrease in Hall mobility at low temperatures and high doping concentrations.

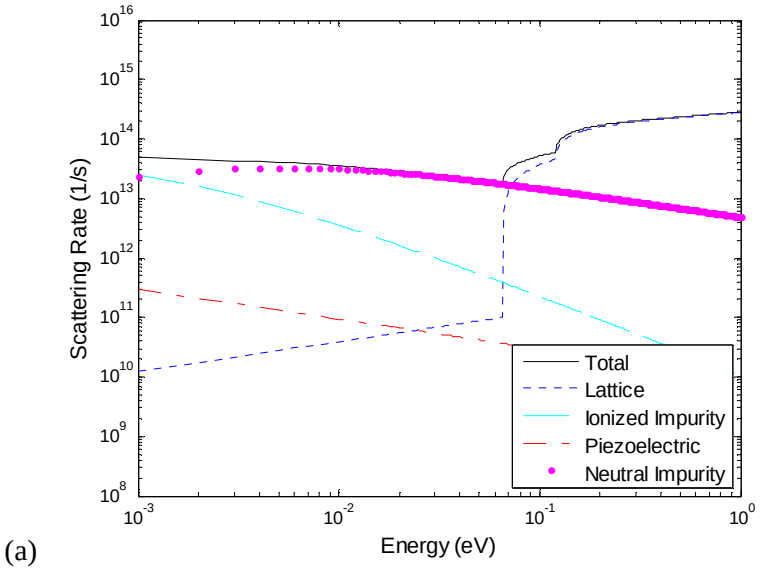

(a)

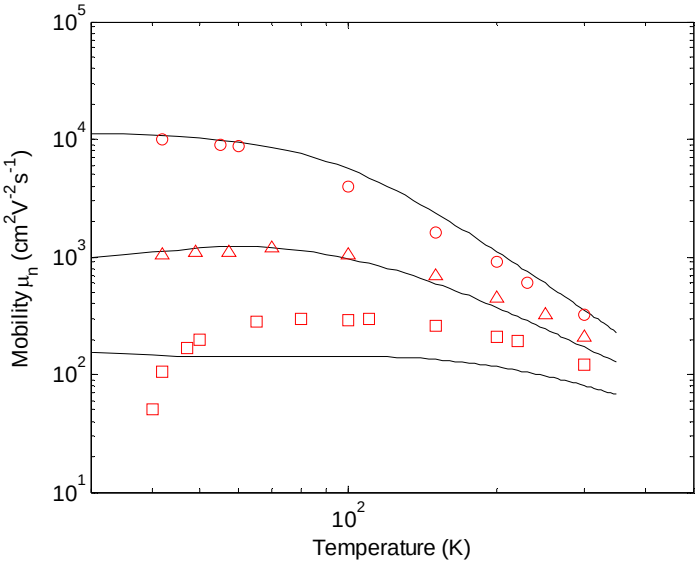

(b)

Fig. 5.6. Effects of ionization energy lowering. (a) Scattering rates versus energy for $N_D = 1 \times 10^{19}\text{cm}^{-3}$ at 30 K. (b) Calculated Hall mobility curves. Parameters the same as those in Fig. 5.3.

CHAPTER 6. CONCLUSION

6.1 Conclusion

In this dissertation, the properties of different polytypes of SiC were studied using computational methods. A novel approach utilizing the EPM with a genetic search algorithm to fit the band structure of 4H-SiC was presented. As more information on the electronic structure of 4H SiC becomes available, this can be a useful method of finding new fitting parameters. This is even more important for the electronic structure of 6H SiC for which almost no experimental data exists.

Next, a more accurate way to obtain the deformation potentials and energies to fit the Hall mobility of 6H SiC was delineated, and the Hall scattering factor was calculated. A similar approach was used before for 4H SiC, but had not yet been applied to 6H SiC. However, further work can be done in trying to obtain a better fit of the band structure of 4H SiC using the above mentioned method.

With the work presented here, a foundation has been laid for further, future computational work. For example, the genetic search algorithm used to fit the band structure of 4H SiC can be applied to 6H SiC when more experimental data becomes available. Indeed, it can be applied to any material to quickly and effectively find satisfactory EPM parameters. In addition, the band structure and the values of the deformation potentials could be used to construct a full band Monte Carlo simulation of SiC devices. In typical Monte Carlo device simulations, a parabolic band approximation is used so that there is no need for the full band structure. However, for the high power applications for which SiC is foreseen to be used in, the large electric fields in these devices result in highly energetic carriers that occupy higher energy states in the conduction band. Simulations under these conditions require a full band approach, requiring the electronic band structure as an input.

REFERENCES

[1] J. Gea-Banacloche and L.B. Kish, "Future directions in electronic computing and information processing," *Proc. IEEE*, vol. 93, pp. 1858-1863, Oct. 2005.

[2] J.B. Casady and R.W. Johnson, "Status of silicon carbide (SiC) as a wide-bandgap semiconductor for high-temperature applications: A review," *Solid-State Electron.*, vol. 39, pp. 1409-1422, Oct. 1996.

[3] P.G. Neudeck, "SiC electronics," in *The VLSI Handbook* New York: CRC & IEEE Press, 2000.

[4] B.J. Baliga, *Silicon Carbide Power Devices*, Hackensack: World Scientific, 2005.

[5] N.W. Ashcroft and N.D. Mermin, *Solid State Physics*, Florence: Brooks Cole, 1976.

[6] P.Y. Yu and M. Cardona, *Fundamentals of Semiconductors*, New York: Springer, 2005.

[7] N.W. Ashcroft, "Electron-ion pseudopotentials in metals," *Phys. Lett. A*, vol. 23, pp. 48-50, Oct. 1966.

[8] M.P. Marder, *Condensed Matter Physics*, New York: John Wiley & Sons, 2000.

[9] H.G. Junginger and W. van Haeringen, "Energy band structure of four polytypes of silicon carbide calculated with the empirical pseudopotential method," *Phys. Stat. Sol.*, vol. 37, pp. 709-719, 1970.

[10] V.I. Gavrilenko, A.V. Postnikov, N.I. Klyui and V.G. Litovchenko, "Energy band structure and optical properties of wurtzite-structure silicon carbide crystals," *Phys. Stat. Sol.*, vol. 162, pp. 477-487, 1990.

[11] C. Persson and U. Lindefelt, "Relativistic band structure calculation of cubic and hexagonal SiC polytypes," *J. App. Phys.*, vol. 82, pp. 5496-5508, Dec. 1997.

[12] B. Wenzien, P. Kackell, F. Bechstedt and G. Cappellini, "Quasiparticle band structure of silicon carbide polytypes," *Phys. Rev. B*, vol. 52, pp. 10897-10905, Oct. 1995.

[13] B. Baumeier, P. Kruger and J. Pollmann, "Self-interaction-corrected pseudopotentials for silicon carbide," *Phys. Rev. B*, vol. 73, 195205, May 2006.

[14] G. Pennington and N. Goldsman, "Empirical pseudopotential band structure of 3C, 4H, and 6H SiC using transferable semiempirical Si and C model potentials," *Phys. Rev. B*, vol. 64, 045104, June 2001.

[15] S.M. Zubkova, L.N. Rusina and E.V. Smelyanskaya, "Temperature dependence of the band structure of 3C, 2H, 4H and 6H SiC polytypes," *Semiconductors*, vol. 37, pp. 257-265, 2003.

[16] W.J. Choyke, D.R. Hamilton and L. Patrick, "Optical properties of cubic SiC: Luminescence of nitrogen-exciton complexes, and interband absorption," *Phys. Rev.*, vol. 133, pp. A1163-A1166, Feb. 1964.

[17] R. Ahuja, A. Ferreira da Silva, C. Persson, J.M. Osorio-Guillen, I. Pepe, K. Jarrendahl, O.P.A. Lindquist, N.V. Edwards, Q. Wahab and B. Johansson, "Optical properties of 4H-SiC," *J. App. Phys.*, vol. 91, pp. 2099-2103, Feb. 2002.

[18] G. Demir, T.E. Renfro, R. Glosser and S.E. Saddow, "Optical characterization of *n*- and *p*-doped 4H-SiC by electroreflectance spectroscopy," *App. Phys. Lett.*, vol. 84, pp. 3540-3542, May 2004.

[19] C. Hammond, *The Basics of Crystallography and Diffraction*, Oxford:Oxford University Press, 2001.

[20] F. Starrost, S. Bornholdt, C. Solterbeck and W. Schattke, "Band-structure parameters by genetic algorithm," *Phys. Rev. B*, vol. 53, pp. 12549-12552, May 1996.

[21] G. Klimeck, R.C. Bowen, T.B. Boykin, C. Salazar-Lazaro, T.A. Cwik and A. Stoica, "Si tight-binding parameters from genetic algorithm fitting," *Superlattices Microstruct.*, vol. 27, pp. 77-88, May-Jun. 2000.

[22] P. Piquini, P.A. Graf and A. Zunger, "Band-gap design of quaternary (In,Ga)(As,Sb) semiconductors via the inverse-band-structure approach," *Phys. Rev. Lett.*, vol. 100, 186403, May 2008.

[23] Y.H. Zheng, "Search target band gap with inverse band structure approach for complex superlattices," *Superlattices Microstruct.*, vol. 48, pp. 343-349, June 2010.

[24] P. Kackell, B. Wenzien and F. Bechstedt, "Influence of atomic relaxations on the structural properties of SiC polytypes from *ab initio* calculations," *Phys. Rev. B*, vol. 50, pp. 17037-17046, Dec. 1994.

[25] M.L. Cohen and T.K. Bergstresser, "Band structures and pseudopotential form factors for fourteen semiconductors of the diamond and zinc-blende structures," Phys. Rev., vol. 141, pp. 789-796, Jan. 1966.

[26] W.R.L. Lambrecht and B. Segall, "Band-structure analysis of the conduction-band mass anisotropy in 6H and 4H SiC," *Phys. Rev. B*, vol. 52, pp. R2249-R2252, July 1995.

[27] M. Lundstrom, *Fundamentals of carrier transport*, Cambridge: Cambridge University Press, 2000.

[28] D.K. Ferry, *Semiconductor Transport*, New York: Taylor & Francis, 2000.

[29] B.K. Ridley, *Quantum Processes in Semiconductors*, Oxford: Oxford Science Publications, 1999.

[30] N.F. Mott, "The electrical resistance of dilute solid solutions," *Proc. Cambridge Philos. Soc.*, vol. 32, pp. 281-290, 1936.

[31] E. Conwell and V.F. Weisskopf, “Theory of Impurity Scattering in Semiconductors,” *Phys. Rev.*, vol. 77, pp. 388-390, Feb. 1950.

[32] H.S.W. Massey and B.L. Moiseiwitsch, “The scattering of electrons by hydrogen atoms,” *Phys. Rev.*, vol. 78, pp. 180-181, Feb. 1950.

[33] C. Erginsoy, “Neutral impurity scattering in semiconductors,” *Phys. Rev.*, vol. 79, pp. 1013-1014, May 1950.

[34] N. Sclar, “Neutral impurity scattering in semiconductors,” *Phys. Rev.*, vol. 104, pp. 1559-1561, May 1956.

[35] J. Bardeen and W. Shockley, “Deformation potentials and mobilities in non-polar crystals,” *Phys. Rev.*, vol. 80, pp. 72-80, Oct. 1950.

[36] G. Arlt and P. Quadflieg, “Piezoelectricity in 3-V compounds with a phenomenological analysis of piezoelectric effect,” *Phys. Stat. Sol.*, vol. 25, pp. 323-330, 1968.

[37] W. Gotz, A. Schoner, G. Pensl, W. Suttrop, W.J. Choyke, R. Stein, and S. Leibenzeder, “Nitrogen donors in 4H-silicon carbide,” *J. Appl. Phys.*, vol. 73, pp. 3332-3338, April 1993.

[38] G. Rutsch, R.P. Devaty, W.J. Choyke, D.W. Langer, L.B. Rowland, E. Niemann, and F. Wischmeyer, “Hall scattering factor and electron mobility of 4H SiC: Measurements and numerical simulation,” *Mater. Sci. Forum*, vol. 338, pp. 733-736, 2000.

[39] J. Pernot, W. Zawadzki, S. Contreras, J.L. Robert, E. Neyret, and L. Di Cioccio, “Electrical transport in n-type 4H silicon carbide,” *J. Appl. Phys.*, vol. 90, pp. 1869-1878, Aug. 2001.

[40] F. La Via, G. Galvagno, F. Roccaforte, A. Ruggiero, and L. Calcagno, “Drift mobility in 4H-SiC Schottky diodes,” *App. Phys. Lett.*, vol. 89, 142105, Oct. 2005.

[41] S. Karmann, W. Suttrop, A. Schoner, M. Schadt, C. Haberstroh, F. Engelbrecht, R. Helbig, and G. Pensl, “Chemical vapor-deposition and characterization of undoped and nitrogen doped single crystalline 6H-SiC,” *J. Appl. Phys.*, vol. 72, pp. 5437-5442, Dec. 1992.

[42] M. Schadt, G. Pensl, R.P. Devaty, W.J. Choyke, R. Stein, and D. Stephani, “Anisotropy of the electron Hall-mobility in 4H, 6H and 15R silicon-carbide,” *Appl. Phys. Lett.*, vol. 65, pp. 3120-3122, Dec. 1994.

[43] H. Iwata and K.M. Itoh, “Donor and acceptor concentration dependence of the electron Hall mobility and the Hall scattering factor in n-type 4H- and 6H-SiC,” *J. Appl. Phys.*, vol. 89, pp. 6228-6234, Jun. 2001.

[44] R. Mickevicius and J.H. Zhao, "Monte Carlo study of electron transport in SiC," *J. Appl. Phys.*, vol. 83, pp. 3161-3167, Mar. 1998.

[45] T. Kinoshita, K.M. Itoh, M. Schadt, and G. Pensl, "Theory of the electron mobility in n-type 6H-SiC," *J. Appl. Phys.*, vol. 85, pp. 8193-8198, Jun. 1999.

[46] S. Dhar and S. Ghosh, "Low field electron mobility in 6H-SiC," *J. App. Phys.*, vol. 88, pp. 6519-6525, Dec. 2001.

[47] G. Rutsch, R.P. Devaty, W.J. Choyke, D.W. Langer, and L.B. Rowland, "Measurement of the Hall scattering factor in 4H and 6H SiC epilayers from 40 to 290 K and in magnetic fields up to 9 T," *J. Appl. Phys.*, vol. 84, pp. 2062-2064, Aug. 1998.

[48] D.L. Rode, "Theory of electron galvanomagnetics in crystals – Hall effect in semiconductors and semimetals," *Phys. Stat. Sol. B*, vol. 55, pp. 687-696, 1973.

[49] D.L. Rode, "Low field electron transport," *Semicond. Semimet.*, vol. 10, pp. 1-89, 1975.

[50] G. Ng, D. Vasileska, D.K. Schroder, "Calculation of the electron Hall mobility and Hall scattering factor in 6H-SiC," *J. Appl. Phys.*, vol. 106, 053719, Sep. 2009.

[51] T. Hill, *An Introduction to Statistical Thermodynamics*, New York: Dover, 1987.

[52] Y. Goldberg, M.E. Levinshtein, S.L. Rumyanstev, *Properties of Advanced Semiconductor Materials: GaN, AlN, InN, BN, SiC, SiGe*, New York:Wiley Interscience, 2001.

[53] A.P. Mirgorodsky, M.B. Smirnov, E. Abdelmounim, T. Merle, and P.E. Quintard, "Molecular approach to the modeling of elasticity and piezoelectricity of SiC polytypes," *Phys. Rev. B*, vol. 52, pp. 3993-4000, Aug. 1995.

[54] K. Kamitani, M. Grimsditch, J.C. Nipko, C.K. Loong, M. Okada, and I. Kimura, "The elastic constants of silicon carbide: A Brillouin-scattering study of 4H and 6H SiC single crystals," *J. Appl. Phys.*, vol. 82, pp. 3152-3154, Sep. 1997.

[55] H. Iwata, K.M. Itoh, and G. Pensl, "Theory of the anisotropy of the electron Hall mobility in n-type 4H- and 6H-SiC," *J. Appl. Phys.*, vol. 88, pp. 1956-1961, Aug. 2000.

[56] G.L. Pearson and J. Bardeen, "Electrical properties of pure silicon and silicon alloys containing boron and phosphorus," *Phys. Rev.*, vol. 75, pp. 865-883, March 1949.

[57] H. Brooks, "Theory of the electrical properties of germanium and silicon," *Adv. Electr. Electron Phys.*, vol. 7, pp. 85-182, 1955.

[58] G.E. Stillman and C.M. Wolfe, "Electrical characterization of epitaxial layers," *Thin Solid Films*, vol. 31, pp. 69-88, 1976.

[59] A. Schoner, N. Nordell, K. Rottner, R. Helbig and G. Pensl, “Dependence of the aluminum ionization energy on doping concentration and compensation in 6H-SiC,” *Inst. Phys. Conf. Ser.*, vol. 142, pp. 493-496, 19